IONIC CONDUCTIVITY OF $Li_{0.5}La_{0.5}Ti_{1-x}Al_xO_3$ ELECTROLYTE LAYER FOR THIN FILM BATTERIES

A Thesis Submitted to
the Graduate School of Engineering and Science of
İzmir Institute of Technology
in Partial Fulfillment of the Requirements for the Degree of

MASTER OF SCIENCE

in Material Science and Engineering

by
Seda ULUSOY

December 2016
İZMİR

We approve the thesis of **Seda ULUSOY**

Examining Committee Members:

Prof. Dr. Lütfi ÖZYÜZER
Supervisor, Department of Physics,
İzmir Institute of Technology

Asist. Prof. Dr. Enver TARHAN
Department of Physics,
İzmir Institute of Technology

Assist. Prof. Dr. Bengi KUTLU
Department of Textile Engineering,
Dokuz Eylül University

21 December 2016

Prof. Dr. Lütfi ÖZYÜZER
Supervisor, Department of Physics,
İzmir Institute of Technology

Assist. Prof. Dr. Gürcan ARAL
Co-advisor, Department of Physics,
İzmir Institute of Technology

Prof. Dr. Mustafa M. DEMİR
Head of the Department of Material Science and Engineering

Prof. Dr. Bilge KARAÇALI
Dean of the Graduate School of Engineering and Sciences

ACKNOWLEDGMENTS

Firstly, I would like to thank my supervisor Prof. Dr. Lütfi Özyüzer for giving me opportunity to write this thesis. Furthermore, I acknowledge him for his excellent guidance, continuous support and understanding throughout my thesis.

I would like to thank also Assoc. Prof. Dr. Gülnur Aygün and Assist. Prof. Dr. Mehtap Özdemir Köklü, who is the project director of this research topic. I would like to thank them for their guidance, support and suggestions during my thesis study. Furthermore, I would like to thank members of my thesis defense committee Asist. Prof. Dr. Enver Tarhan and Assist. Prof. Dr. Bengi Kutlu for giving suggestions and helpful comments.

I also would like to acknowledge 'The Scientific and Technological Research Council of Turkey (TÜBİTAK)' as this project is supported by TÜBİTAK with the project number 114M044 during my experimental studies and thanks to AQUREC (Applied Quantum Research Center) and Center for Materials Research (CMR) at IZTECH for providing research facilities such as XRD and SEM. Moreover, I would like to express my thanks to Teknoma Technological Materials Inc. for providing indium tin oxide (ITO) substrates for the thin film growth.

I am very thankful to all of my lab mates and friends; Yasemin, Hürrriyet, Hasan, Fulya, Ayten, Hakan, Dilara, Ece, Şehriban, Hatice, Gülşah and all members of office Z-46.for sharing their knowledge and friendship. Moreover, I cannot pay my debt to my dear friend Safa whose help and support is always beside me.

Last but not least, I wish to express my cordial appreciation to my family for their love, generous care and consistent support during my education. I am exceptionally fortunate to be blessed with a perfect family

ABSTRACT

IONIC CONDUCTIVITY OF $Li_{0.5}La_{0.5}Ti_{1-x}Al_xO_3$ ELECTROLYTE LAYER FOR THIN FILM BATTERIES

In this study, crystalline lithium lanthanum titanium (aluminum) oxide $Li_{0.5}La_{0.5}Ti_{1-x}Al_xO_3$ (LLTO) powder targets with different Aluminum (x) content were prepared by conventional solid state reactions as $Li_{0.5}La_{0.5}TiO_3$, $Li_{0.5}La_{0.5}Ti_{0.99}Al_{0.01}O_3$, $Li_{0.5}La_{0.5}Ti_{0.95}Al_{0.05}O_3$, $Li_{0.5}La_{0.5}Ti_{0.90}Al_{0.10}O_3$ and $Li_{0.5}La_{0.5}Ti_{0.85}Al_{0.15}O_3$ compositions. Then, after a couple of calcination processes with regrinding of the prepared stoichiometric powder batch, it is placed into Cu-base plate to be pressed in order to provide a compact, dense and smooth target surface for the thin film deposition. For the thin film fabrication, radio frequency (RF) magnetron sputtering technique is used to sputter the dielectric target. Thin films were deposited on soda-lime glass (SLG) and 256 nm thick indium tin oxide (ITO) layer grown on soda-lime glass (SLG) substrates. For the electrical measurements of LLTO thin film, it was fundamental to have ITO as conducting layer electrode. Targets with various Al (x) compositions were deposited for the investigation of Ti substitution with Al on structural and electrical properties. Besides, crystalline structure of the targets was characterized by X-ray powder diffraction (XRPD) and Raman Spectroscopy analysis while structural, morphological and compositional properties of the thin films were determined by x-ray diffraction (XRD), scanning electron microscope (SEM) and x-ray photoelectron spectroscopy (XPS) respectively. Moreover, in order to understand the effect of Al doping on ionic conductivity, electrical measurements were performed at room temperature by AC impedance spectroscopy forming ITO/LLTO/Al capacitor like structure. Maximum ionic conductivity result is obtained for $Li_{0.5}La_{0.5}Ti_{0.95}Al_{0.05}O_3$ thin film composition. Also, temperature dependent ionic conductivity measurements were performed from 298 K to 373 K to evaluate activation energy for the Li-ion conduction.

Keywords: Ionic conductivity, $Li_{0.5}La_{0.5}Ti_{1-x}Al_xO_3$, electrolyte, thin film, activation energy, RF magnetron sputtering

ÖZET

İNCE FİLM PİLLER İÇİN $Li_{0.5}La_{0.5}Ti_{1-x}Al_xO_3$ ELEKTROLİT KATMANININ İYONİK İLETKENLİĞİ

Bu çalışmada, kristal yapıdaki lityum lantanum titanyum (alüminyum) oksit $Li_{0.5}La_{0.5}Ti_{1-x}Al_xO_3$ (LLTO) bileşimi çeşitli Alüminyum (x) kompozisyonlarında $Li_{0.5}La_{0.5}TiO_3$, $Li_{0.5}La_{0.5}Ti_{0.99}Al_{0.01}O_3$, $Li_{0.5}La_{0.5}Ti_{0.95}Al_{0.05}O_3$ ve $Li_{0.5}La_{0.5}Ti_{0.90}Al_{0.10}O_3$, $Li_{0.5}La_{0.5}Ti_{0.85}Al_{0.15}O_3$ kompozisyonları olmak üzere katı hal reaksiyonları sonucu hazırlanmıştır. Hazırlanan stokiyometrik karışımlar, maruz bırakıldığı birkaç kalsinasyon işleminin ardından yoğun ve düzgün bir yüzeye sahip bir hedef yüzeyi elde etmek için bakır-altlığa yerleştirilmiş ve preslenerek ince film üretimi için hazır hale getirilmiştir. İnce film üretimi içinse radyo frekansı mıknatıssal saçtırma tekniği ile dielektrik hedef malzemesi SLG ve 256 nm kalınlıktaki indiyum kalay oksit (ITO) kaplı camlar üzerine saçtırılmıştır. LLTO ince filmlerinin elektriksel ölçümleri için ITO elektrodu kullanılmıştır. Farklı Al (x) kompozisyonuna sahip filmler alüminyumun (Al) titanyum ile yer değiştirmesinin araştırması yapılarak, yapısal ve elektriksel özellikleri incelenmiştir. Bunların yanısıra, hedeflerin kristal yapısı, x-ışını kırınımı ve Raman spektroskopisi ile karakterize edilirken, ince filmlerin yapısal, morfolojik ve kompozisyona dair özellikleri sırasıyla x-ışını kırınımı, taramalı uç elektron mikroskopu ve x-ışını fotoelektron spektroskopisi ile belirlenmiştir. Buna ek olarak Al katkılamasının iyonik iletkenliğe etkisini anlamak için, ITO/LLTO/Al kapasitör yapısı oluşturularak oda sıcaklığında AC empedans spektroskopisi ile elektriksel ölçümler yapılmıştır. En yüksek iyonik iletkenlik değeri $Li_{0.5}La_{0.5}Ti_{0.95}Al_{0.05}O_3$ ince film kompozisyonuna aittir. Aynı zamanda, sıcaklığa bağlı iyonik iletkenlik ölçümleri 298 K'den 372 K' e kadar olan sıcaklık aralığında her 10 derecede bir farklı sıcaklık değerleri için kaydedilmiş ve Li iyonunun iletimi için gereken aktivasyon enerjisi hesaplanmıştır.

Anahtar sözcükler: İyonik iletkenlik, $Li_{0.5}La_{0.5}Ti_{1-x}Al_xO_3$,elektrolit,ince film, aktivasyon enerjisi, RF mıknatıssal saçtırma

To my lovely family

TABLE OF CONTENTS

LIST OF FIGURES ix

LIST OF TABLES xii

LIST OF SYMBOLS xiv

CHAPTER 1 INTRODUCTION 1

1.1. Brief History of Li-ion Batteries 3
1.2. Solid State Electrolytes 3
1.3. Working Principle of a Conventional Li-ion Cell 6

CHAPTER 2 IONIC CONDUCTION 8

2.1. Mechanism of Ionic Conduction 8
2.2. AC Circuit Theory and Representation of Complex Impedance Values 9
2.2.1. Lissajous Pattern 13
2.3. Impedance Data Representations 14
2.3.1. Nyquist plot 14
2.3.1. Bode Plot 15
2.3.2. Cole-Cole Plot 16
2.4. Anomalies in Experimental Impedance Spectroscopy Data 16

CHAPTER 3 EXPERIMENTAL PROCEDURE 18

3.1. Target Preparation 18
3.1.1. Calcination 20
3.1.2. Sintering 21
3.1.3. Hydraulic Press 22
3.2. Thin Film Fabrication Method 23
3.2.1. RF Magnetron Sputtering 23

3.2.2. Heat Treatment of the Thin Films 25
3.2.3. Thermal Evaporation 25
3.3. Characterization of the Targets and the Thin Films 27
3.3.1. Structural and Morphological Analysis 27
3.3.2. Electrical Characterization of the Thin Films 28

CHAPTER 4 RESULTS AND DISCUSSION 30
4.1. Characterization of the $Li_{0.5}La_{0.5}Ti_{1-X}Al_xO_3$ Targets Prepared by Conventional Solid State Reactions 30
4.1.1. X-ray Powder Diffraction Analysis 30
4.1.2. Raman Spectroscopy 31
4.2. Characterization of the $Li_{0.5}La_{0.5}Ti_{1-x}Al_xO_3$ Thin Films 36
4.2.1. X-ray Diffraction 36
4.2.2. Scanning Electron Microscopy (SEM) 37
4.2.2.1. Surface Morphology of Different $Li_{0.5}La_{0.5}Ti_{1-X}Al_xO_3$ Thin Film Compositions 38
4.2.2.2. Effect of Anneal Temperature on Each Composition of $Li_{0.5}La_{0.5}Ti_{1-X}Al_xO_3$ Thin Films 40
4.2.3. X-ray Photoelectron Spectroscopy 47
4.2.4. Electrochemical Impedance Spectroscopy (EIS) 51
4.2.4.1. Change in Electrical Properties with Increasing Film Thickness, for Different Compositions 51
4.2.4.2. Effect of Composition on Ionic Conduction 56
4.2.4.3. Effect of Anneal Temperature on Different Compositions 59
4.2.4.4. Arrhenius Plot 62
4.2.4.5. Frequency Dependent Conductivity Measurements 63

CHAPTER 5 CONCLUSION 66

REFERENCES 68

LIST OF FIGURES

Figure **Page**

Figure 1.1 Types of batteries according to their electrolyte types 3
Figure 1.2. Arrhenius plots of electrical conductivity of perovskite-type lithium lanthanum titanate among several well-known solid state Li ion conductors 4
Figure 1.3. Parts of conventional solid state battery during intercalation processes. 7
Figure 2.1. . Homogeneous sample bounded by two electrodes..... 10
Figure 2.2 Sinusoidal voltage input V and a current response that shifted in phase in a typical impedance experiment 12
Figure 2.3. Impedance data representation: (A) Lissajous Figure, (B) complex impedance plots 14
Figure 2.4. Example of a Nyquist plot with impedance vector 15
Figure 2.5. Bode plot representation showing information of the frequency 15
Figure 2.6. Complex impedance plane plot showing tipped straight line at low frequencies. 17
Figure 2.7.Typical changes in the complex plane figure if the values of the two capacitances are not sufficiently different from each other. 17
Figure 3.1. Flow chart of target preparation of $Li_{0.5}La_{0.5}Ti_{1-x}Al_xO_3$ with different stoichiometric amounts of Al_2O_3 19
Figure 3.2. Schematic diagram of the heat treatment stages for calcination process. 20
Figure 3.3. There stages of solid state sintering on a microscopic scale (1) particle bonding initiated at contact points (2) contact points grow into necks (3) pores between particles reduced in size. 21
Figure 3.4. Schematic diagram of the heat treatment stages for sintering..... 21
Figure 3.5 Hydraulic press (a) and the powder target pressed in Cu-base plate (b)…...22
Figure 3.6. Cylindrical button for pelletizing (a) and the pellets both side covered with Ag-paste 23
Figure 3.7. The picture of sputter chamber (a) and plasma during RF sputtering (b). ... 24
Figure 3.8. Schematic diagram of annealing procedure for T = 100, 200, 300, 400 ˚C..25
Figure 3.9. Schematic representation of thermal evaporation setup..... 26
Figure 3.10. Cross-sectional view of the sample after Aluminum evaporation 27

Figure 3.11. Top view of the mask (a) and LLTO thin film sample after Aluminum is evaporated (b) 27
Figure 3.12. AC impedance spectroscopy measurement setup with probe station and monitor showing probes on the sample from (a) top view and (b) cross-sectional view of the sample. 29
Figure 4.1. XRD patterns of all $Li_{0.5}La_{0.5}Ti_{1-x}Al_xO_3$ targets, which are expressed as nominal compositions of $Li_{0.5}La_{0.5}TiO_3$ (pure), $Li_{0.5}La_{0.5}Ti_{1-x}Al_xO_3$ (x=0.01, 0.05, 0.10, 0.15)..... 31
Figure 4.2. Raman spectroscopy results of the targets with different Al (x) compositions 32
Figure 4.3. Raman spectra of slowly cooled (SC) and quickly cooled (QC) LLTO The inset shows complex impedance plot of the same SC and QC samples. 33
Figure 4.4. XRD patterns of $Li_{0.5}La_{0.5}TiO_3$ (pure) target and films according to that targets with anneal treatments in air for 2 h at 100, 200, 300 and 400 °C and the crystalline peaks of the ITO substrate. 36
Figure 4.5. Schematic representation of the two adjacent grains and the grain boundary between them 38
Figure 4.6. SEM image of the surface of (a) $Li_{0.5}La_{0.5}TiO_3$ thin film without Al_2O_3 addition (b) thin film obtained from $Li_{0.5}La_{0.5}Ti_{1-x}Al_xO_3$ (x=0.01) (c) from$Li_{0.5}La_{0.5}Ti_{1-x}Al_xO_3$ (x=0.05) (d) $Li_{0.5}La_{0.5}Ti_{1-x}Al_xO_3$ (x=0.10) (e) $Li_{0.5}La_{0.5}Ti_{1-x}Al_xO_3$ (x=0.15) targets deposited by RF magnetron sputtering on ITO/SLG substrates and the SEM image of (f) ITO substrate. 39
Figure 4.7 XPS spectra of $Li_{0.5}La_{0.5}TiO_3$ (pure) and $Li_{0.5}La_{0.5}Ti_{1-x}Al_xO_3$ for different x-compositions of x = 0.05, x = 0.10 and x = 0.15 ..... …47
Figure 4.8 XPS spectra of $Li_{0.5}La_{0.5}Ti_{1-x}Al_xO_3$ thin films with various x-content labeled as pure, 0.05, 0.10 and 0.15 from La 3d region..... 48
Figure 4.9. XPS spectra of $Li_{0.5}La_{0.5}Ti_{1-x}Al_xO_3$ thin films with various x-content labeled. as pure, 0.05, 0.10 and 0.15 from Ti 2p region. 49
Figure 4.10 XPS spectra of $Li_{0.5}La_{0.5}Ti_{1-x}Al_xO_3$ thin films withvarious x-content labeled as pure, 0.05, 0.10 and 0.15 from Al 2p region. 49

Figure 4.11 XPS spectra of $Li_{0.5}La_{0.5}Ti_{1-x}Al_xO_3$ thin films with various x-content labeled as pure, 0.05, 0.10 and 0.15 from O 1s region. 50
Figure 4.12 $Li_{0.5}La_{0.5}Ti_{1-x}Al_xO_3$ (x = 0.00 – pure) thin film with thicknesses proportional to their deposition times on ITO/SLG s 53
Figure 4.13. $Li_{0.5}La_{0.5}Ti_{1-x}Al_xO_3$ (x = 0.01) thin film with various thicknesses deposited for 30 and 60 minutes on ITO/SLG substrates. 54
Figure 4.14 $Li_{0.5}La_{0.5}Ti_{1-x}Al_xO_3$ (x = 0.05) thin film with various thicknesses deposited for 30 and 60 minutes on ITO/SLG substrates. 54
Figure 4.15. $Li_{0.5}La_{0.5}Ti_{1-x}Al_xO_3$ (x = 0. 10) thin films with various thicknesses deposited for 15, 30, 60 and 90 minutes on ITO/SLG substrates 55
Figure 4.16. The complex impedance spectra of as deposited $Li_{0.5}La_{0.5}Ti_{1-x}Al_xO_3$ thin films with different Al contents. 57
Figure 4.17 Schematic representation of Aluminum substituted content (x) versus ionic conductivity results obtained from thin film samples. 58
Figure 4.18 Arrhenius plots of the conductivity as a function of 1000/T for LLTAlO (x=0.05) annealed at 300 K and the inset shows complex impedance curves at each temperature. 63
Figure 4.19. Frequency dependence of the hopping conductivity for different potential energy profiles: (a) periodic constant activation energy, (b) single bi-well, (c) potential profile with multiple activation energies ... 64
Figure 4.20. Real part (σ') of complex conductivity as a function of frequency for $Li_{0.5}La_{0.5}Ti_{1-x}Al_xO_3$ (x=0.05) annealed at 300 ˚C from 25 ˚C to 110 ˚C in 0.1 Hz – 200 kHz frequency range 64

LIST OF TABLES

Table **Page**

Table 1.1. LLTO compounds with various modifications in composition and substitution of ions in the bulk form 5

Table 3.1 Targets with different nominal compositions of Al (x) and weight percentage of Al_2O_3 inside the powder mixture. 22

Table 4.1. Observed modes and attributions for different x- compositions of powder target samples..... 34

Table 4.2. Grain size averages of different $Li_{0.5}La_{0.5}Ti_{1-x}Al_xO_3$ compositions of pure (x = 0.00), x = 0.01, x = 0.05, x = 0.10, and x = 0.15. 39

Table 4.3. SEM images of surfaces of as deposited $Li_{0.5}La_{0.5}TiO_3$ thin film and $Li_{0.5}La_{0.5}TiO_3$ thin films annealed at 100 ˚C, 200 ˚C, 300 ˚C, and 400 ˚C with 500 nm, 1µm scales and grain size average. 41

Table 4.4. SEM images of surfaces of as deposited $Li_{0.5}La_{0.5}Ti_{1-x}Al_xO_3$ (x=0.01) thin film and $Li_{0.5}La_{0.5}Ti_{0.99}Al_{0.01}O_3$ thin films annealed at 100 ˚C, 200 ˚C, 300 ˚C, and 400 ˚C with 1µm, 2/3µm scales and grain size average..... 42

Table 4.5. SEM images of surfaces of as deposited $Li_{0.5}La_{0.5}Ti_{1-x}Al_xO_3$ (x=0.05) thin film and $Li_{0.5}La_{0.5}Ti_{0.95}Al_{0.05}O_3$ thin films annealed at 100 ˚C, 200 ˚C, 300 ˚C, and 400 ˚C with 1µm scale and grain size average. 44

Table 4.6. SEM images of surfaces of as deposited $Li_{0.5}La_{0.5}Ti_{1-x}Al_xO_3$ (x=0.10) thin film and $Li_{0.5}La_{0.5}Ti_{0.90}Al_{0.10}O_3$ thin films annealed at 100 ˚C, 200 ˚C, 300˚C, and 400 ˚C with 1µm scale and grain size average. 45

Table 4.7. SEM images of surfaces of as deposited $Li_{0.5}La_{0.5}Ti_{1-x}Al_xO_3$ (x=0.15) thin film and $Li_{0.5}La_{0.5}Ti_{0.85}Al_{0.15}O_3$ thin films annealed at 100 ˚C, 200 ˚C, 300 ˚C, and 400 ˚C with 500 nm, 1µm scale and grain size average. 46

Table 4.8. Deposition time and thickness variables for $Li_{0.5}La_{0.5}TiO_3$ (pure) thin film deposition process 52

Table 4.9. Comparison results of the deposition time and conductivity for each composition (except for $Li_{0.5}La_{0.5}Ti_{1-x}Al_xO_3$ (x = 0.15)) 52

Table 4.10. Room temperature conductivities for different chemical compositions of $LiLaTiO_3$ 56

Table 4.11. Ionic conductivities measured at room temperature from different nominal chemical compositions of thin films. 57
Table 4.12. Complex impedance plots of each $Li_{0.5}La_{0.5}Ti_{1-x}Al_xO_3$ composition with anneal treatment 60

LIST OF SYMBOLS

C	Capacitance	Farad
d	Parallel distance between the plates	cm
A	Area of the parallel plates	cm^2
Q	Charge	Coulomb
V	Voltage	V
I	Current	A
R	Resistance	ohm
Z	Impedance	ohm.cm
k_B	Boltzmann constant = $8.617\ 343(15)\times10^{-5}$ $eV.K^{-1}$	$eV.K^{-1}$
Ea	Activation energy	eV
f	frequency	Hz
χ_c	Capacitive reactance	ohm
T	Temperature	K
j	Current density	mA/cm^2
h	Planck constant	$m^2kg.s^{-1}$
p	momentum	$kg.m.s^{-1}$

Greek Letters

ε_o	Permittivity of vacuum (free space) $\sim8.85\times 10^{-12}$ $F\cdot m^{-1}$	$F\cdot m^{-1}$
ε_r	Relative permittivity/ dielectric constant	-
ρ	Resistivity	ohm.cm
σ	Conductivity	$S.cm^{-1}$
ω	Angular frequency	rad/s
φ	Phase shift	rad
τ	Characteristic relaxation time	
λ	de Broglie wavelength	m

CHAPTER 1

INTRODUCTION

Due to the increasing demand of energy sources, it is crucial to develop energy in a way that the environment is protected and gives response to demands of today's living standards such as higher energy density, longer lifespan, flexible and lightweight designs (Tarascon and Armand 2001). All solid state batteries have attracted much attention to bring solutions for the new improvements. For instance, commonly used liquid electrolytes have begun to fail because of the safety concerns like leakage and pollution, although they serve a high ionic conductivity at room temperature. Therefore, lithium ion conducting solid electrolytes have received substantial interest because of their significant advantages such as absence of leakage and pollution, thermal stability, resistance to shocks and vibrations, and miniaturization capability (Zheng et al. 2014).

Especially by the thin film applications of all solid state batteries, it is possible to provide higher volumetric and gravimetric energy densities. Electrolyte layer inside the battery, which is responsible for the ionic conduction through the anode and cathode regions during the intercalation process, which has a crucial importance to determine system performance in terms of charge/discharge rate, power density and efficiency. The main function of the electrolyte layer is to provide high ionic conduction at room temperature, but also low electronic conductivity to prevent short circuit. The first compound of this solid electrolyte family was synthesized by Belous et al. (Belous 1996), their outstanding room temperature lithium conductivity confirmed by Inaguma et al. (Inaguma et al. 1993) is about 10^{-3}S/cm. Since then, much attention has been paid to the ABO_3 perovskite type compound $Li_{3x}La_{(2/3)-x}\square_{(1/3)-x}TiO_3$ (LLTO) and its structurally related modifications to enhance its ionic conductivity. Inaguma et al. (Inaguma et al. 1994) has reported that the lithium lanthanum titanate with perovskite structure show high ionic conductivity of the bulk part as $1x10^{-3}$ S/cm at room temperature. The reason for this high ionic conduction is explained by the presence of vacancies on the A-site of the lattice which allows Li^+ ion to move freely through the vacant sites of the ABO_3 perovskite LLTO structure. Furthermore, it is also understood that perovskite structure can tolerate having different valence states on A-site and B-site that enables to develop

substitutional structure modifications like Al substitution for Ti to increase ionic conductivity like in our research topic. In the study of Morata-Orrantia et al. (Morata-Orrantia, Garcıa-Martin, and Alario-Franco 2003) $La_{2/3}Li_xTi_{1-x}Al_xO_3$ was examined as bulk structure with compositions of x = 0.1, 0.2, 0.3 and for x = 0.25, ionic conductivity was calculated as 7.6 x 10^{-5} S.cm^{-1} at room temperature, which proves that Al substitution has a positive effect on ionic conduction up to some level. As reduction of Ti^{4+} to Ti^{3+} at low potentials cause short circuit by the electronic conduction that takes place during the intercalation process (Geng et al. 2009).So with the light of this knowledge, it is necessary to prevent reduction. Therefore, substitution of Ti cation for Aluminum that has less tendency toward reduction against Li metal compared to Ti become our focus in this research. Besides, lower effective ionic radii of Al^{3+} (r_{Al}^{3+} =0.53Å) compared to Ti^{4+} (r_{Ti}^{4+} = 0.605 Å) enables to less reduction caused by the Li metal which explains the increase in ionic conductivity by Al substitution (Morata-Orrantia et al. 2002). Furthermore, to optimize lithium conductivity special focus on composition-structure and ionic conductivity properties were studied by Youmbi et al. (Youmbi et al. 2012) and found that $Li_{0.5}La_{0.5}TiO_3$ composition has shown the highest ionic conductivity as 1.7x10^{-3} S.cm^{-1} among $Li_{0.34}La_{0.51}TiO_{2.94}$, $Li_{0.27}La_{0.59}TiO_3$, $Li_{0.34}La_{0.56}TiO_3$ (cubic), $Li_{0.34}La_{0.56}TiO_3$ (tetragonal), $Li_{0.10}La_{0.63}TiO_3$ compositions that have Li ion conductivities down to 7.9 x 10^{-5} S.cm^{-1}.

So, $Li_{0.5}La_{0.5}TiO_3$ composition is chosen as our starting material, later by aluminum substitution $Li_{0.5}La_{0.5}Ti_{1-x}Al_xO_3$ samples were synthesized with different x compositions (x = 0.01, x = 0.05, x = 0.10, x = 0.15). Those prepared powder samples, after some steps of conventional solid state reactions, were pressed in a Cu-base plate in order to form a ceramic powder target for the RF magnetron sputtering process. $Li_{0.5}La_{0.5}Ti_{1-x}Al_xO_3$ (LLTAlO) thin films were deposited on ITO/SLG substrate under pure Ar atmosphere. ITO/SLG is preferred as a substrate to obtain contact from the back side of the thin film electrolyte for the impedance measurements to determine ionic conductivities. Furthermore, for the structural characterizations, SEM, XRD, Raman and XPS analysis were done to explain the relationship between the ionic conduction and the structure of the thin films.

1.1. Brief History of Li-ion Batteries

Lithium-ion (Li-ion) batteries were first introduced into the marketplace by Sony in 1991 to power a video camera. Since then, Li-ion batteries have become part of our daily lives—powering a wide range of mobile electronic devices and power tools. Then, by the developments in the 1980s developments of portable electronic devices such as video cameras, laptops and mobile phones led to a growing need for rechargeable batteries with greater capacity, reduces size and weight for that given capacity (Yoshino 2012). Although lead-acid, nickel- cadmium as well as nickel-metal hydrides are in use for the demand of rechargeable batteries previous to Li-ion battery technology, they cannot provide reduction in size and weight for higher energy storage capacities.

1.2. Solid State Electrolytes

Generally, batteries can be classified under two categories such as primary and rechargeable (secondary) battery types according to electrolyte types.

	Aqueous electrolyte battery	Nonaqueous electrolyte battery (high voltage, capacity)
Primary battery (disposable)	Mn dry cell, Alkaline dry cell	Metallic lithium battery
Secondary battery (rechargable)	Lead acid battery, Nickel- Cadmium battery, Nickel-metal hydride battery	Lithium-ion battery

Figure 1.1 Types of batteries according to their electrolyte types (Source: Yoshino 2012)

Here, it can be referred that electrolytes are one of the key components of a Li-ion battery. Current electrolytes are the result of many years of research that play a key role in providing good performance for applications. New and more challenging battery requirements for power tools, hybrid electric vehicles, plug-in electric vehicles, and stand

by power sources for communications and modern airplanes require a significant developments in battery chemistry. It is necessary for a battery to have higher energy densities provided by higher gravimetric and volumetric energy density considerations. The batteries needed are often of higher voltages and higher energy content. Furthermore, they will be exposed to extremes of temperature with the necessity of still providing long cycle and storage life and for the user's safety. A new class of electrolytes is needed to meet these demands. The new electrolytes must not only provide good ionic conduction over a wide range of ambient temperatures but also provide good chemical stability and compatibility with the more reactive electrode materials that are required to achieve higher battery specific energy and power. With the demand for higher energy density

The electrolyte formulations must meet the demanding criterion necessary for long-term battery operation (high stability with selective reactions, high safety, etc.). Conductivity remains an important consideration for high-power applications (Jow et al. 2014).

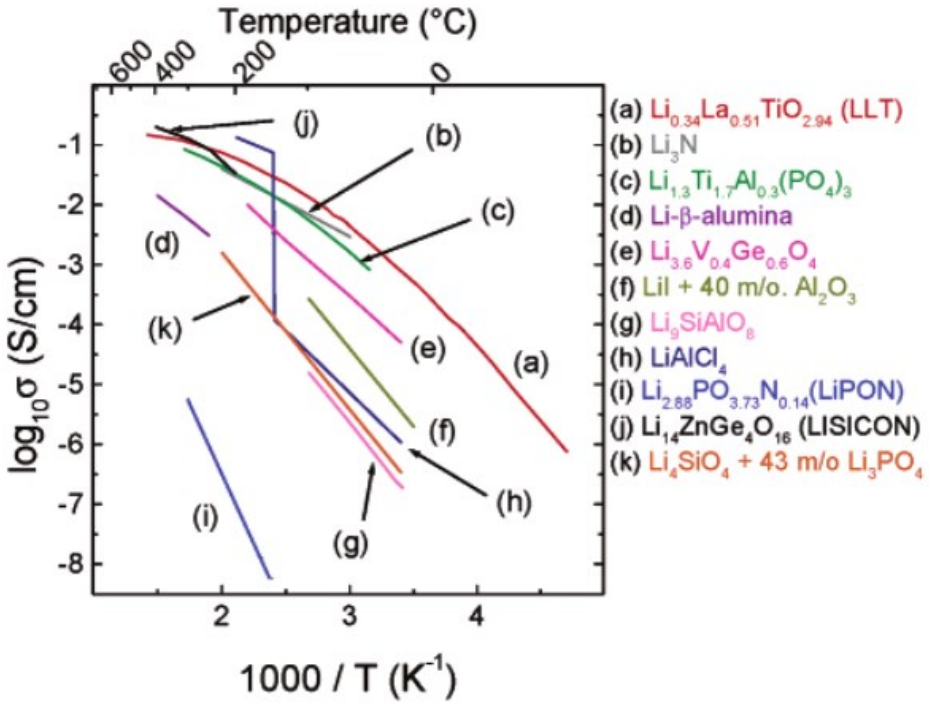

Figure 1.2. Arrhenius plots of electrical conductivity of perovskite-type lithium lanthanum titanate among several well-known solid state Li ion conductors (Source: Stramare, Thangadurai, and Weppner 2003).

There is plenty of solid state electrolyte material compounds to be a good candidate for the demand of higher energy density devices. Here, from the Figure 1.3,

conductivity of those compounds are represented. Their conductivity depending on temperature plot, which is called as Arrhenius plot are shown.

From the Figure 1.3., it can be observed that Li0.34La0.51TiO2.94 (LLTO) has the highest ionic conducting compound within that temperature range. Especially, it is important to note that it has its highest ionic conducting property at room temperature, which is the challenge that we face in solid state Li-ion conductors.

Rely on this high ionic conductivity result among those materials, $Li_{0.34}La_{0.51}TiO_{2.94}$ has become a hot topic. In the Table 1.1, it can be seen that various compositions of LLTO and also different kinds of substitutional changes are investigated. It should be highlighted that Al substitution has a great impact on ionic conduction compared to other species.

Table 1.1. LLTO compounds with various modifications in composition and substitution of ions in the bulk form (Source: Stramare, Thangadurai, and Weppner 2003)

Compounds	**σ_{bulk} (S/cm)**	**E_a (eV)**
$Li_{0.34}La_{0.51}TiO_{2.94}$	1.0×10^{-3}	0.40
$Li_{0.27}La_{0.59}TiO_3$	6.8×10^{-4} $\perp$ *c-axis*	0.36
	5.8×10^{-4} $\parallel$ *c-axis*	0.35
$Li_{0.34}La_{0.56}TiO_3$ (*cubic, a_p*)	1.53×10^{-3}	0.33
$Li_{0.34}La_{0.56}TiO_3$ (*tetragonal, a_p, $2a_p$*)	6.88×10^{-4}	0.35
$Li_{0.10}La_{0.63}TiO_3$	7.9×10^{-5}	0.36
$(Li_{0.1}La_{0.5})_{0.9}Sr_{0.1}TiO_3$	1.5×10^{-3}	
$Li_{0.15}La_{0.51}Sr_{0.15}TiO_3$	5.3×10^{-5}	0.38
$Li_{0.25}La_{0.41}Sr_{0.25}TiO_3$	7.6×10^{-5}	0.35
$(Li_{0.1}La_{0.63})(Mg_{0.5}W_{0.5})O_3$	$\sim 10^{-6}$	0.39
$(La_{0.5}Li_{0.5})_{1-x}(La_{0.5}Na_{0.5})_xTiO_3$ *(x>0.4)*	$<10^{-7}$	
$(La_{0.5}Li_{0.5})_{1-x}(La_{0.5}Na_{0.5})_xTiO_3$ *(x=0.25)*	2×10^{-5}	
$Li_{0.5}(La_{0.4}Nd_{0.1})TiO_3$	$\sim 10^{-3}$	0.33
$Li_{0.245}La_{0.592}Ti_{0.98}Mn_{0.02}O_3$	$\sim 10^{-3}$	
$La_{0.58}Li_{0.36}Ti_{0.95}Mg_{0.05}O_3$	2.1×10^{-4}	0.29
$La_{0.56}Li_{0.36}Ti_{0.95}Al_{0.05}O_3$	6.4×10^{-4}	0.26
$La_{0.55}Li_{0.36}Ti_{0.95}Mn_{0.05}O_3$	1.9×10^{-4}	0.29

(cont. on next page)

Table 1.1. (cont.)

$La_{0.55}Li_{0.36}Ti_{0.95}Ge_{0.05}O_3$	3.6×10^{-4}	0.29
$La_{0.55}Li_{0.36}Ti_{0.95}Ru_{0.05}O_3$	5.2×10^{-5}	0.28
$La_{0.51}Li_{0.36}Ti_{0.95}W_{0.05}O_3$	7.3×10^{-4}	0.27
$La_{0.54}Li_{0.36}TiO_3$	8.9×10^{-4}	0.29
$La_{0.55}Li_{0.36}Ti_{0.995}Al_{0.005}O_3$	1.1×10^{-3}	0.28
$Li_{0.067}La_{0.64}TiO_{2.99}$	7.9×10^{-5}	0.36
$Li_{0.06}La_{0.66}Ti_{0.93}Al_{0.06}O_3$	1.7×10^{-6}	0.36
$Li_{0.10}La_{0.66}Ti_{0.90}Al_{0.10}O_3$	7.3×10^{-6}	0.35
$Li_{0.15}La_{0.66}Ti_{0.85}Al_{0.15}O_3$	9.6×10^{-6}	0.36
$Li_{0.20}La_{0.66}Ti_{0.80}Al_{0.20}O_3$	4.3×10^{-5}	0.33
$Li_{0.25}La_{0.66}Ti_{0.75}Al_{0.25}O_3$	7.7×10^{-5}	0.35
$Li_{0.30}La_{0.66}Ti_{0.70}Al_{0.30}O_3$	1.7×10^{-5}	0.33
$La_{(1/3)-x}Li_{3x}NbO_3$		
$x = 0.01$	4.06×10^{-6}	0.36
$x = 0.02$	2.33×10^{-5}	0.33
$x = 0.03$	3.52×10^{-5}	0.35
$x = 0.04$	4.25×10^{-5}	0.37
$x = 0.05$	3.85×10^{-5}	0.36
$x = 0.06$	3.82×10^{-5}	0.34
$La_{0.67-x}Na_{1.5x}TiO_3$		
$x = 0.08$	$<10^{-7}$	0.92
$x = 0.14$	$<10^{-7}$	0.92
$Li_{0.25}La_{0.25}TaO_3$	1.4×10^{-5}	0.35

1.3. Working Principle of a Conventional Li-ion Cell

First of all, each battery is made up of many smaller batteries called cells. Just in every other battery, there is a positive and negative electrode called cathode and the anode. Cathode (positive electrode) is generally made of a very pure Li-metal oxide. The more uniform its chemical composition, it will have better performance and provide longer battery life. The anode (negative electrode), which is located on the other side of

Li-ion cell, is made of graphite in form of carbon layers. Moreover, the battery is filled with a transport medium, so that the Li-ions carrying batteries charge can flow freely, which is called as electrolyte (separator). This electrolyte layer must also be extremely pure, and as free of water as possible in order to ensure efficient charging to prevent the short circuit.

When the battery is charging, positively charged Li-ions pass from cathode through the separator into the layered graphite structure of the anode, where it is stored during this charging process.

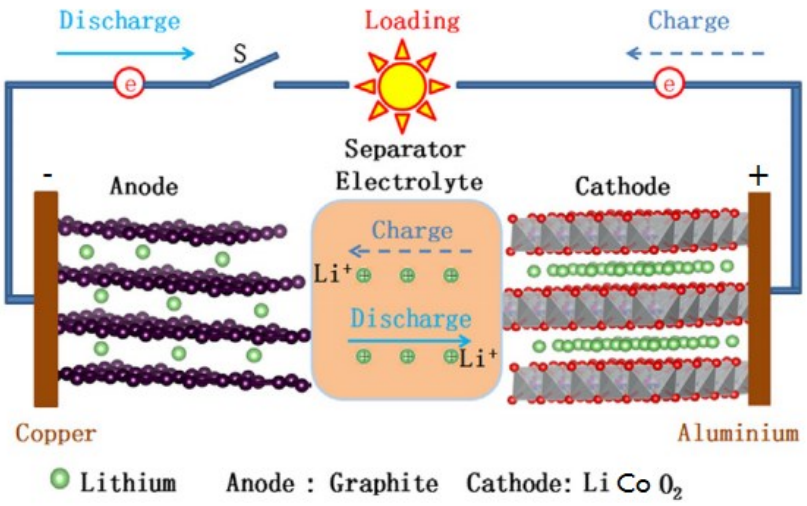

Figure 1.3. Parts of conventional solid state battery during intercalation processes.

When the battery is discharging, that is; the energy is removed from the cell as current to perform work out of the battery. During this intercalation process, Li-ions travel via the electrolyte from anode to the cathode as it can be seen from Figure 1.3.

So, the amount of energy available to get from a Li-ion cell strongly depends on the quality of the materials used. To sum it all up, higher quality, pure materials among with customized formulations will lead to a longer battery life and better battery performance.

CHAPTER 2

IONIC CONDUCTION

2.1. Mechanism of Ionic Conduction

Ionic conduction depends on the presence of vacant sites into which ions can move. In the absence of a field, thermal vibrations proportional to $k.T$ may cause ions and vacancies to exchange sites. The Nernst–Einstein equation links this process of self-diffusion with the ion drift σ_i caused by an electric field:

$$\frac{\sigma_i}{D_i} = \frac{N_i Q_i}{k.T} \tag{2.1}$$

where D_i is the self- or tracer-diffusion coefficient for an ion species i, Q_i is the charge it carries and N_i is its concentration (Moulson A.J. 2014). Features that contribute to ionic mobility are small charge, small size and favorable lattice geometry. A highly charged ion will polarize, and be polarized by the ions of opposite charge as it moves past them, and this will increase the height of the energy barrier that inhibits a change of site. The movement of a large ion will be hindered in a similar way by the interaction of its outer electrons with those of the ions it must pass between in order to reach a new site. Some structures may provide channels which give ions space for movement. The presence of vacant sites assists conduction since it offers the possibility of ions moving from neighboring sites into a vacancy which, in consequence, moves in the opposite direction to the ions. This is particularly likely in the case of the oxygen lattice since the smaller cations do not present large energy barriers impeding the process.

All of the above statements can be generalized for the ion conduction in crystals. However, structure might be glassy (amorphous) structure or a mixed phase. In practice ceramics are usually multiphase, consisting of crystalline phases, glasses and porosity. The overall behavior depends on the distribution as well as the properties of these constituents. If the minor phase is conductive it can greatly reduce the resistivity of the composite or, if insulating, it can reduce its conductivity. Also, an abrupt change in the

mode of conduction at the main phase–intercrystalline phase boundary may introduce barriers to conduction that dominate the overall electrical behavior.

To conclude, in crystalline ionic conductors, charge transport occurs via lattice defects, frequently vacancies, and dependence of conductivity on temperature is observed. The common glassy or vitreous materials encountered, conduct ions by the migration through the random glass network. Finally, it is important to appreciate that, for most ceramics encountered, the conduction mechanism is far from fully understood, as the structure consist of multi-phase nature. Probably it will involve a combination of ionic and electronic charge carriers, and the balance will depend upon temperature and ambient atmosphere. The effects of impurity atoms may well dominate the conductivity and there is also the complication of contributions, perhaps overriding, from grain boundaries and other phases – glass, crystalline or both.

2.2. AC Circuit Theory and Representation of Complex Impedance Values

Impedance which corresponds the complex electrical resistance is similar concept with electrical resistance R. It is the ability of a circuit element to resist the flow of electrical current. It is based on the analysis of current response to small sinusoidal perturbation in potential and defined by the ratio between input voltage V and output current I:

$$R=V/I \quad \text{(Ohm's Law)} \tag{2.2}$$

Although this is a well-known relationship, its use is limited to only one circuit element- ideal resistor. An ideal resistor has several basic properties:

- It obeys Ohm's law at all current, voltage and AC frequency levels.
- Its resistance value is independent of frequency.
- AC current and voltage signals are in phase with each other.

However, the real world contains circuit elements that show much more complex behavior. Therefore, impedance takes place of the simple concept of resistance in order to express a more general circuit parameter.

To analyze a sample material, which is ideally homogeneous and completely fills the volume bounded by two electrodes with a visible area A, that are placed apart from each other with a uniform distance d, as shown in Figure 2.1. When external voltage V is applied, a uniform current, *I* passes through the sample, and the resistance is defined as:

$$R = \rho.\frac{d}{A} \tag{2.3}$$

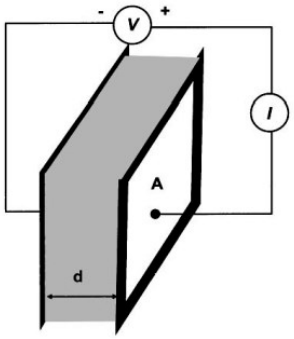

Figure 2.1. Homogeneous sample bounded by two electrodes

where ρ [ohm.cm] is the characteristic electrical resistivity of a material, representing its ability to resist the passage of the current. The inverse of resistivity is conductivity σ [1 / ρ (ohm .cm)] or [S/cm], reflecting the material's ability to conduct electrical current between two bounding electrodes.

Resistivity of the thin film material would be defined by the resistance value, which is the result obtained from complex impedance plot that cuts the x-axis of the impedance plot which corresponds to real part of impedance value, independent from frequency.

$$\rho = R.\frac{A}{d} \tag{2.4}$$

which is the reverse of conductivity, σ. So, the conductivity can be expressed as follows:

$$\sigma = \frac{1}{\rho} = \frac{d}{R \times A} \tag{2.5}$$

An ideal resistor can be replaced in the circuit by another ideal element that completely rejects any flow of current. This element can be an "ideal" capacitor like in our case. When two bounding electrodes are separated by a non-conducting

(or "dielectric") medium is formed, AC current and voltage signal will be this time out of phase with each other. Capacitance is the ability to store an electrical charge. The value of capacitance will be represented as follows; (Lvovich 2012)

$$C = \frac{Q}{V} = \varepsilon_o . \varepsilon_r . \frac{A}{d} \tag{2.6}$$

where *C :* capacitance [Farad, F], *A* : area of the electrode [cm^2], *d :* separation between the electrodes [cm], ε_o : constant electrical permittivity of free space (8.85×10^{-14} F/cm), and ε_r : relative permittivity/ dielectric constant [unit less].

Permittivity is a measure of resistance that is encountered when forming electric field inside the medium. Although the word 'permit' suggests inverse quantity, it is the materials ability to resist electric field (Callister 8 Ed.).

$$\varepsilon_r = \frac{\varepsilon}{\varepsilon_o} \tag{2.7}$$

Dielectric constant or relative permittivity indicates how easily a material can become polarized by the imposition of an electric field. ε_r (vacuum) = 1, but when the dielectric medium is inserted between the plates instead of vacuum, $\varepsilon_r > 1$, which means that the charge storing capacity is increased.

By a typical EIS experiment, material characteristics such as resistivity, conductivity and permittivity can be determined. Impedance is a more general concept than either pure resistance or capacitance, as it takes the phase differences between the input voltage and output current into account. Like resistance, impedance is the ratio between voltage and current, demonstrating the ability of a circuit to resist the flow of electrical current, represented by the "real impedance" term, but it also reflects the ability of a circuit to store electrical energy, reflected in the "imaginary impedance" term. Impedance can be defined as a complex resistance encountered when current flow through a circuit composed of various resistors, capacitors, and inductors.

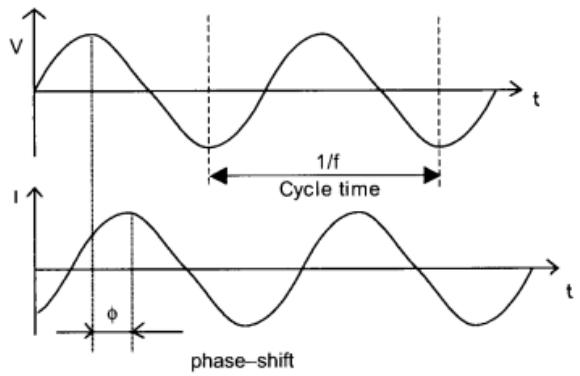

Figure 2.2 Sinusoidal voltage input V and a current response that shifted in phase in a typical impedance experiment

AC voltage signal is generally used to excite for electrochemical impedance measurements. The voltage signal *V(t)* is expressed as a function of time *t*, has the form:

$$V(t) = V_A.sin\ (2.\pi.f.t) = V_A.sin\ (\omega t) \tag{2.8}$$

Radial frequency ω is an expression for the applied AC frequency *f* in radians, that has the unit radians/second as $\omega=2\pi f$.

The current response to that sinusoidal voltage input will also be a sinusoid but this time shifted in phase (ϕ).

$$I(t) = I_A.sin\ (\omega t + \phi) \tag{2.9}$$

Impedance of the system can be explained by the analogy to Ohm's law;

$$Z^* = \frac{V(t)}{I(t)} = \frac{V_A.\sin(\omega t)}{I_A.\sin(\omega t+\phi)} = Z_A.\frac{\sin(\omega t)}{\sin(\omega t+\phi)} \tag{2.10}$$

where $Z_A = |Z|$, and the phase shift, ϕ. If we plot the applied sinusoidal voltage signal on the x-axis of a graph and the sinusoidal response signal *I(t)* on the y-axis, an oval shape called "Lissajous figure" will appear which can be seen in Figure 2.3. (A).

2.2.1. Lissajous Pattern

Lissajous figures appear on oscilloscope screens was the accepted method of impedance measurement prior to lock-in amplifiers and frequency response analyzers. Today's modern equipment enables us to apply voltage input with variable frequencies and collecting the output impedance responses as the frequency is changing from lower to higher frequencies.

Using Euler's relationship which is,

$$e^{j\phi} = cos\phi + jsin\phi \tag{2.11}$$

It is possible to express impedance as a complex function. The potential V(t) can be described as:

$$V(t) = V_A.e^{j\omega t} \tag{2.12}$$

and the current response is;

$$I(t) = I_A. .e^{j\omega t - j\phi} \tag{2.13}$$

So, the impedance can be expressed as complex number that consist of 'real' or in phase (Z_{real}) and 'imaginary', or out of phase (Z_{im}) part as in Figure 2.3. (B).

$$Z^* = \frac{V}{I} = Z_A.e^{j\phi} = Z_A.(cos\phi + jsin\phi) = Z_{real} + Z_{im} \tag{2.14}$$

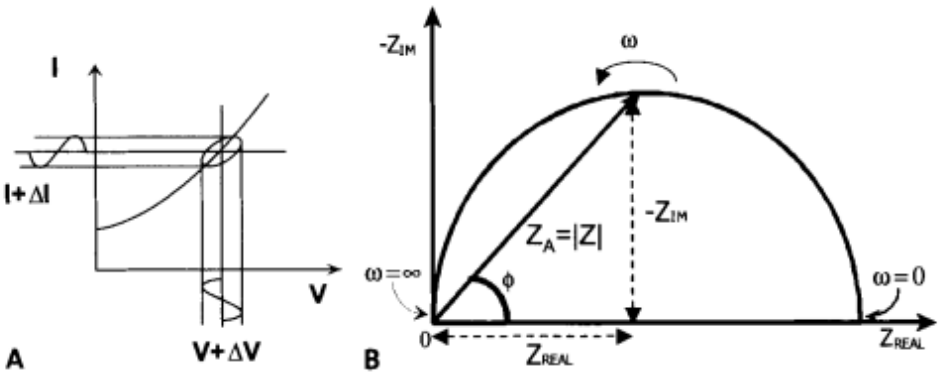

Figure 2.3. Impedance data representation: (A) Lissajous Figure, (B) complex impedance plots

2.3. Impedance Data Representations

As in the case of any other spectroscopic analysis the separate responses may overlap and the experimental curve must then be resolved into its separate constituent semicircles (remember Lissajous figure is the combination of voltage and current signal).

2.3.1. Nyquist plot

There are various data representations to interpret impedance data signal. One of the common complex data representation is 'Nyquist plot' which is expressed as $Z(\omega)$ consist of a real and an imaginary part. The real part is plotted on x-axis and the imaginary part on y-axis of the chart which can be seen from Figure 2.4. Each point of the Nyquist plot indicates the impedance at one frequency. From right to left side of the plot, frequency is increasing (Stoynov, Vladikova, and Academy 2009).

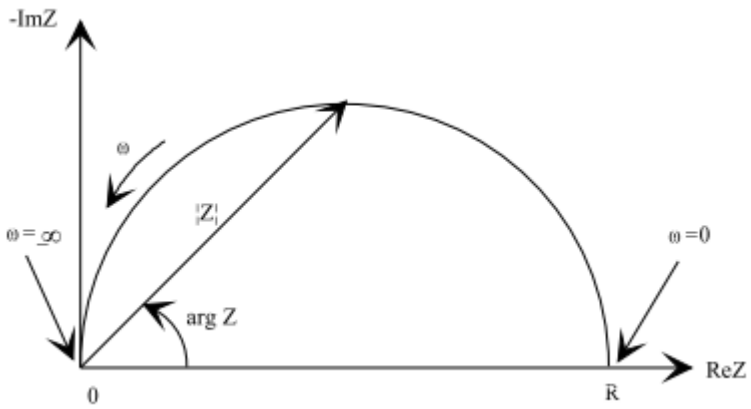

Figure 2.4. Example of a Nyquist plot with impedance vector

One disadvantage of Nyquist plot is that it does not visualize at what frequency the data is recorded. But it can be plotted also as a function of frequency for further interpretation related with frequency.

2.3.1. Bode Plot

In this representation, impedance is plotted with log frequency on the x-axis and both absolute values of the impedance and the phase shift on the y-axis. Unlike the Nyquist Plot, Bode Plot shows the frequency information.

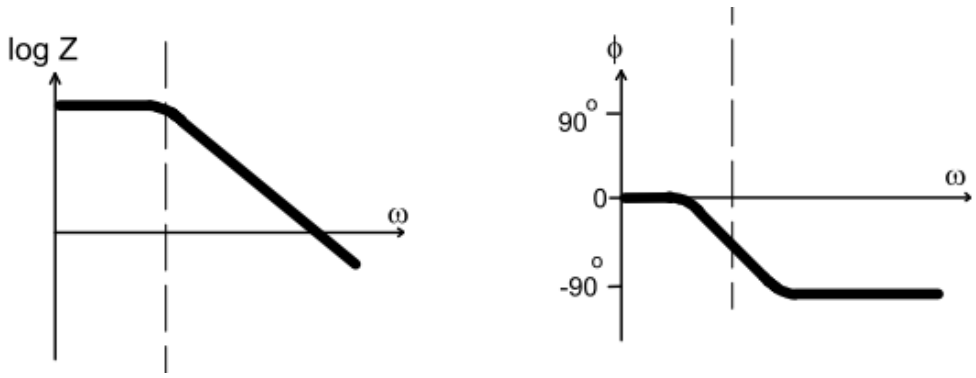

Figure 2.5. Bode plot representation showing information of the frequency

2.3.2. Cole-Cole Plot

Cole-Cole function was used to fit the dielectric spectra of the investigated ceramics is expressed as follows;

$$\tilde{\varepsilon} = \varepsilon_{\infty} + \frac{\Delta\varepsilon}{1+(i\omega\tau)^{1-\alpha}} \tag{2.15}$$

where ε_{∞} is the high frequency permittivity of the studied process, $\Delta\varepsilon$ is the dielectric strength, $\omega = 2\pi f$ is the angular frequency, τ is the characteristic relaxation time and α is a parameter between 0 and 1, that describes deviation from Debye-type behavior.
Complex impedance and complex dielectric diagrams enables to study the variation of both real and imaginary parts of different dielectric functions by the change in frequency (García-Martín et al. 2009).

So, within the light of this theoretical knowledge, experimental studies are carried as it is explained in the following chapter. After the experimental procedure, characterization tools are used to define the sample characteristic and interpretation of the physical background that the experimental results tell us.

2.4. Anomalies in Experimental Impedance Spectroscopy Data

During the impedance measurements, it is assumed that there is no significant electronic conductivity in the solid electrolyte phase and ionic species are completely blocked at the electrolyte/electrode interface. Actually this is not the case that occurs in the experimental results. Therefore, perfect semi- circle shape cannot be observed in experimental analysis. There are some reasons that may be offered as reason for anomalies. For instance, a common experimental observation is that the low frequency tail in complex impedance plots is not truly vertical, but is a straight line inclined at a finite angle from vertical, at lower frequency region. A typical representation of this experimental data behavior can be seen in Figure 2.6. It is related with processes occur at the solid electrolyte interface (Conway 1991), (Huggins 2002).

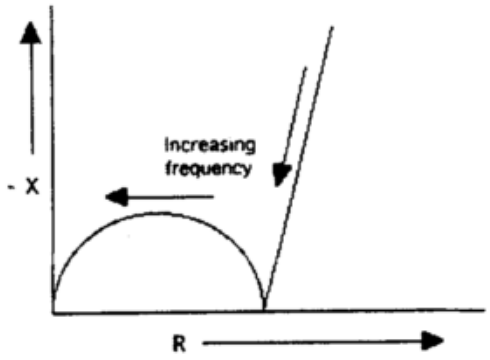

Figure 2.6. Complex impedance plane plot showing tipped straight line at low frequencies. (Source: (Huggins 2002))

Besides, distortion of the semi-circle shape as like in Figure 2.7., is another type of anomaly in impedance measurements. The impedance does not go all the way down to the real axis at the intermediate frequencies, if the values of parallel plate capacitor (C_{geom}), and the contribution of capacitive properties of the two electrolyte/electrode interface (C_{int}) are not so sufficiently different from each other (Raistrick, Ho, and Huggins 1976). It generally results from the use of electrode that has poor contact with the solid electrolyte. So, roughness of the thin film layer of electrode and electrolyte interface play an important role.

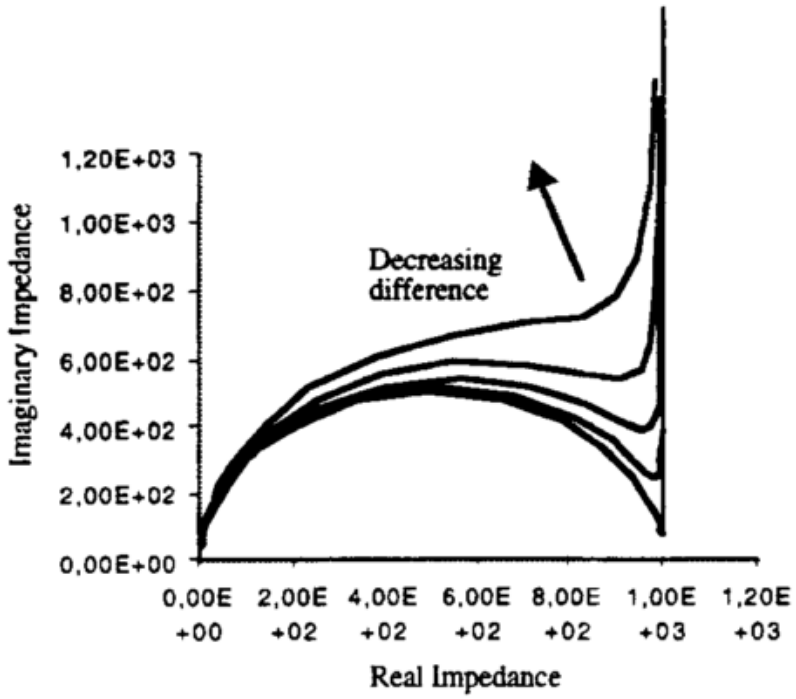

Figure 2.7.Typical changes in the complex plane figure if the values of the two capacitances are not sufficiently different from each other.(Source: (Huggins 2002))

CHAPTER 3

EXPERIMENTAL PROCEDURE

Experimental procedure can be divided into three parts. In the first part, target preparation step for the thin film deposition process, is explained in terms of conventional solid state reactions like calcination, sintering and apart from them pelletizing with a hydraulic press. Second part is the thin film deposition process using RF magnetron sputtering. In the last part, structural, morphological and electrical measurements conducted on a number of different compositions of $Li_{0.5}La_{0.5}Ti_{1-x}Al_xO_3$ (x=0, 0.01, 0.05, 0.10, 0.15) targets and thin film compounds will be described.

3.1. Target Preparation

The $Li_{0.5}La_{0.5}TiO_3$ pure and $Li_{0.5}La_{0.5}Ti_{1-x}Al_xO_3$ aluminum doped targets were prepared by conventional solid state reactions from stoichiometric amounts of Li_2CO_3 (Sigma Aldrich, 99.997 %), La_2O_3 (Sigma Aldrich, 99.999 %), TiO_2 (Sigma Aldrich, > 99.5 %), and Al_2O_3 (Sigma Aldrich, > 99.999 %) powders. The batch of powders were mixed inside agata mortar with a pestle for 6 hours in order to obtain a homogeneous mixture for the calcination process. Then, the stoichiometric mixture of the powders was placed in an alumina crucible boat and calcined 3 times at 1200 ^oC in air for 6 hours to expel CO_2 gas. After every step of calcination powder was grinded. The calcined batch was poured in a 2-inch circular Cu base plate ground and pressed with a cylindrical button at 5 MPa and sintered at 600 ^oC for 1 h in air to have a compact and solid mass form for the sputtering process. In addition, for Al_2O_3 (Sigma Aldrich, 99.99%) added powder mixtures almost same procedure was applied except that Al_2O_3 powder is added to powder mixture after the second calcination step, it is grinded and third calcination is performed again at 1200 ^oC for 6 hours in a box furnace in air environment (Gülen 2015). The produced LLTO targets were placed into the sputter gun of the vacuum chamber to grow LLTO thin films using RF magnetron sputtering technique.

Stoichiometric ratio followed during the target preparation is like as follows;

(0.25 mole) Li_2CO_3 + (0.25 mole) La_2O_3 + (1-x) TiO_2 + (x/2) Al_2O_3 → $Li_{0.5}La_{0.5}Ti_{1-x}Al_xO_3$ + CO_2

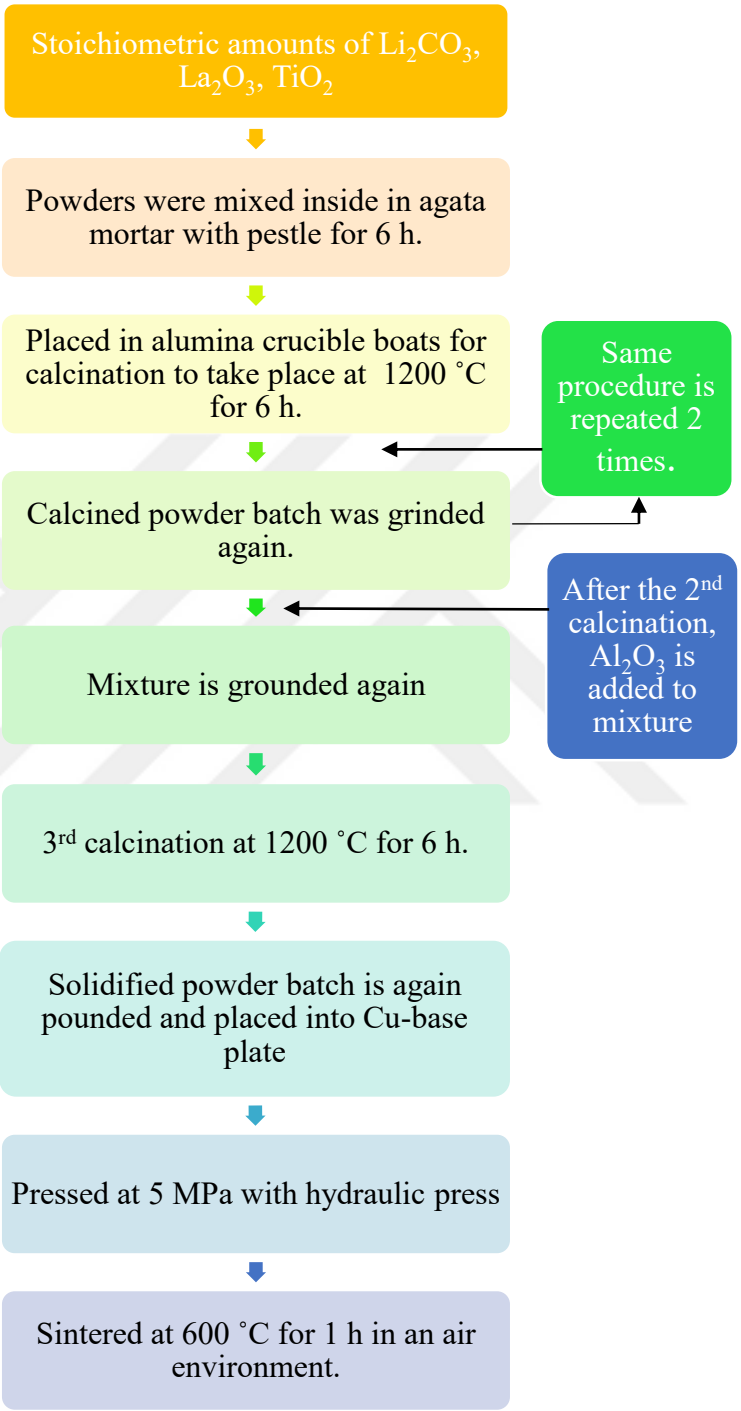

Figure 3.1. Flow chart of target preparation of $Li_{0.5}La_{0.5}Ti_{1-x}Al_xO_3$ with different stoichiometric amounts of Al_2O_3

3.1.1. Calcination

Calcination is heating of a solid to a high temperature value, which is below its melting point, to create a condition of thermal decomposition or phase transformation rather than melting. It also enables to drive off the volatile matter, which can be named as decarbonataion that decomposes CO_2 in a gas form from the chemical compound which provides a proper condition for the desired composition to be formed. Beside these, it is also possible to increase particle size and reduce the specific surface area of the chemical components that comes into a conventional solid state reaction.

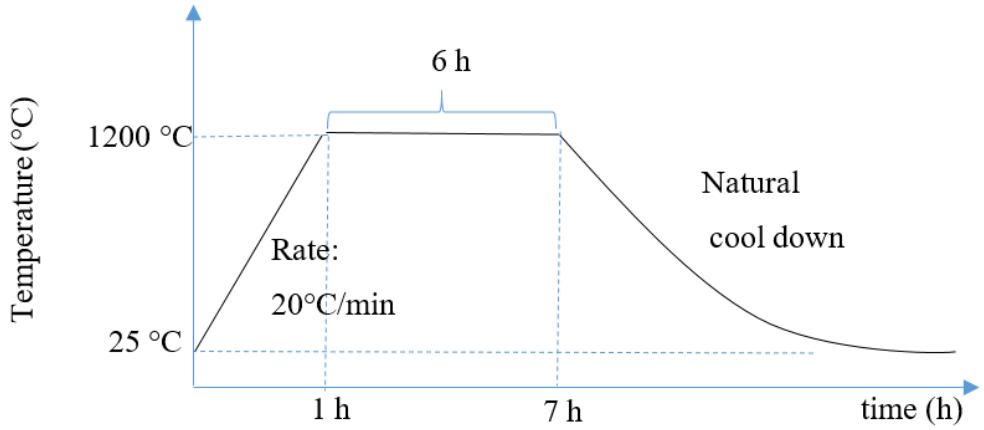

Figure 3.2. Schematic diagram of the heat treatment stages for calcination process.

In Figure 3.2., it can be seen schematic diagram of our heat treatment stages on LLTO target powder for the calcination process, which is applied in an air environment in a box furnace. From room temperature, powder batch inside alumina crucible boats are heated with a heating rate of 20 °C/min up to 1200 °C. Then, the powder batch is calcined at 1200 °C. for 6 hours and after leaved to natural cool down process.

3.1.2. Sintering

Sintering is generally referred as densification process. It aims to produce denser components after sintering process. Here in Figure 3.3, there stages of sintering can be clearly seen. In the first step, particle bonding is only initiated at the contact points, as the diffusion is triggered by the increase in temperature during the sintering, contact points will grow into necks and finally pores between the intra particles will be reduced.

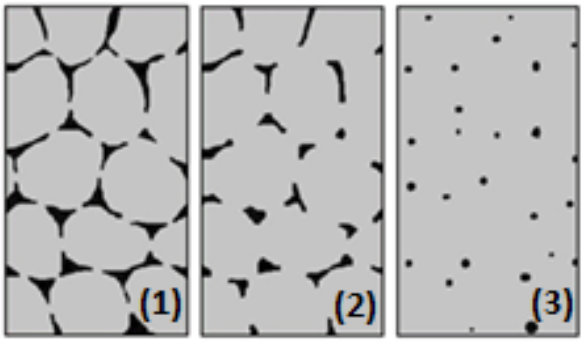

Figure 3.3. There stages of solid state sintering on a microscopic scale (1) particle bonding initiated at contact points (2) contact points grow into necks (3) pores between particles reduced in size. (Retrieved from: http://www.pm-review.com/introduction-to-powder-metallurgy/sintering-in-the-powder-metallurgy-process/)

During our experimental procedure, schematic representation in Figure 3.4. is followed for the sintering process that takes place in air environment.

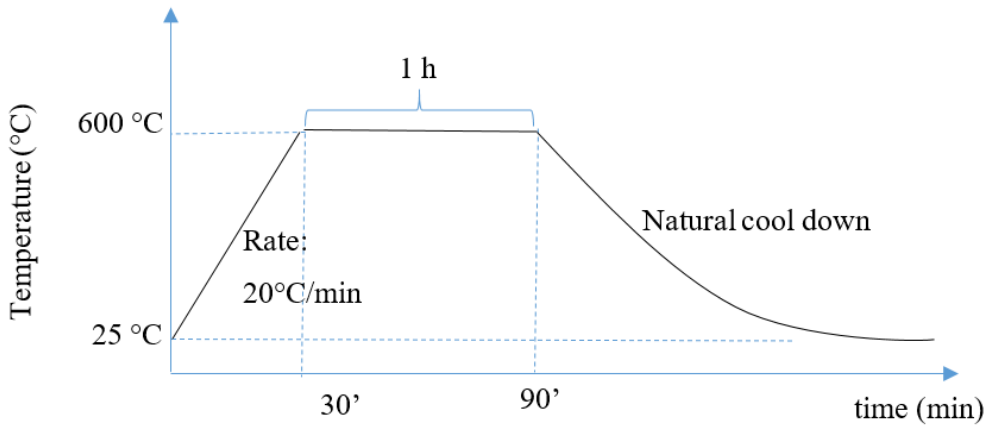

Figure 3.4. Schematic diagram of the heat treatment stages for sintering

Table 3.1 Targets with different nominal compositions of Al (x) and weight percentage of Al_2O_3 inside the powder mixture.

$Li_{0.5}La_{0.5}Ti_{1-x}Al_xO_3$	% weight of Al_2O_3
x = 0.00 (pure)	% 0.00
x = 0.01	% 0.28
x = 0.05	% 1.4
x = 0.10	% 2.8
x = 0.15	% 4.3

3.1.3. Hydraulic Press

Before the sintering process, calcined powder batch is placed in a Cu-base plate to be placed inside the sputter gun. Before, it is placed inside the chamber for the deposition, it should be pressed to have a uniform, denser surface for the sputtering process. So, powder placed in Cu- base plate is pressed at 5 MPa with a hydraulic press machine in Figure 3.5. Then, it is ready for the sintering to take place.

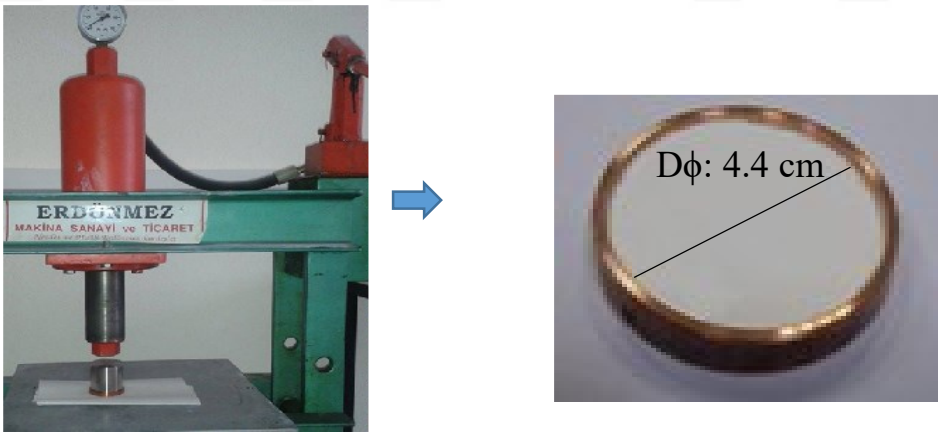

(a) (b)

Figure 3.5 Hydraulic press (a) and the powder target pressed in Cu-base plate (b).

Also for the bulk conductivity measurements, pellets were prepared by a cylindrical button can be seen from Figure 3.6.(a), (b) with Ag paste on both sides.

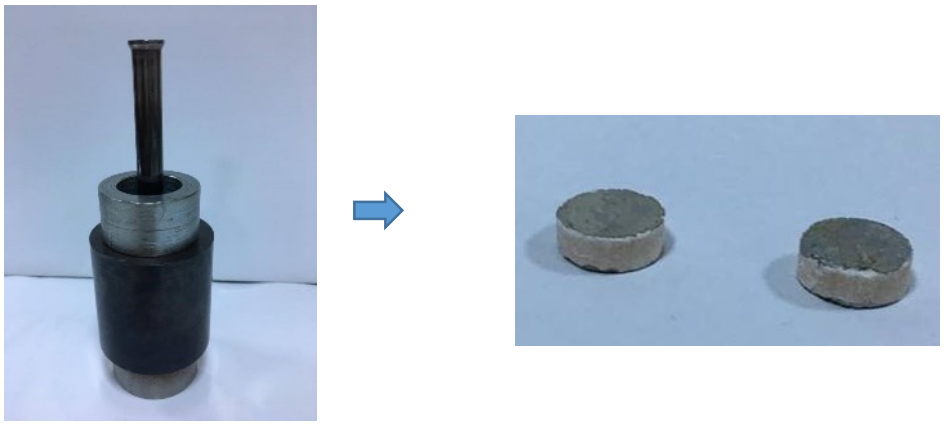

(a) (b)

Figure 3.6. Cylindrical button for pelletizing (a) and the pellets both side covered with Ag-paste

3.2. Thin Film Fabrication Method

3.2.1. RF Magnetron Sputtering

Magnetron sputtering is used to deposit prepared targets on ITO /SLG substrates. As the target material is a dielectric material that has high resistivity (ρ) values usually greater than~ 10^{12} Ω.cm. At least to draw a current density j of 1mA/cm^2, a voltage $V = \rho jd$ should be applied across the target. Assuming the thickness of the target, d is equal to 0.1 cm, $V = \rho jd$ equation tells that ~10^9 V should be applied, which is an impossible high voltage value. In other words, target resistivity exceeding~ 10^6 Ω.cm cannot be DC sputtered, high voltage will cause it to burn instead of sputtering it. To overcome this problem, RF (AC) puttering is used because dielectric-filled capacitors' impedance will drop by increasing frequency (Ohring 2001). By making use of this fact, radio frequency (f = 10^2-10^8 Hz) voltage signal can be applied. So, unlike the resistance which has a fixed value, for AC voltage signal the resistance case is different, it is called reactive capacitance for a dielectric, which is in our case the target that we used for the sputtering. Here, is the formula of reactive capacitance that can be dropped by the increasing frequency value which is radio frequency for this sputtering process.

$$\text{Capacitive reactance} \rightarrow X_C = \frac{1}{2\pi f C} \tag{3.1}$$

So, by RF magnetron sputtering system, dielectric targets that have different amounts of Aluminum inside the composition, have sputtered on ITO/SLG substrates by applying 96 W forward bias voltage. The pressure of the chamber is evacuated to prevent any impurity gas atom to join in deposition. For this purpose, rough pump is used. After the pressure of the chamber has dropped to 10^{-3} Torr by rough pump, turbo molecular pump is turned on to lower the pressure inside the chamber. Pressure value 10^{-6} Torr is reached and then the chamber is ready for the sputtering process. To create plasma environment, 50 sccm inert Argon (Ar) gas is sent into chamber. Ar atoms collide with electrons inside the chamber are ionized. Especially around the target region which is provided by the magnets placed around target. These magnets creating magnetic field around the target, gathers the electrons around target and provide more collision of Ar atoms with electrons to form Ar^+ ions.

$$Ar + e^- \rightarrow Ar^+ + 2e^-$$

In Figure 3.7.(b), glow discharge which we call plasma can be seen. Also, substrate holder on top of the plasma can be realized. Substrate holder was placed parallel to the target holder which are located 13 cm apart from each other. Substrate holder was heated up 220 ˚C in order to have thin films with larger grain sizes. Beside, working pressure during deposition is equal to 4.73 mTorr.

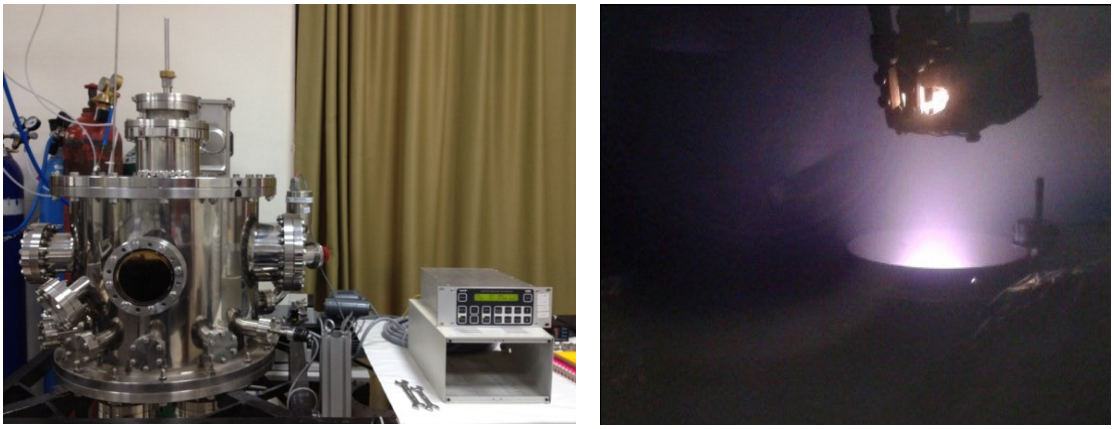

(a) (b)

Figure 3.7. The picture of sputter chamber (a) and plasma during RF sputtering (b).

3.2.2. Heat Treatment of the Thin Films

While the microstructure of the thin films can be controlled by the heat treatment steps, microstructure can rule the properties of the material. Heating of a material over a long time span that enables strains and cracks to be removed or at least can provide stress relaxation inside the material. It also allows atoms to diffuse inside the structure and rearrange itself to form crystalline structure by annealing. Especially for this study, electrical properties of LLTO thin films highly depend on the microstructure. So, in order to improve these properties, appropriate heat treatment steps of 100 ˚C, 200 ˚C, 300 ˚C and 400 ˚C anneal procedure is applied to have a control on grain size and morphology. Furthermore, it is aimed to get rid of stress inside the thin film samples, if there is any.

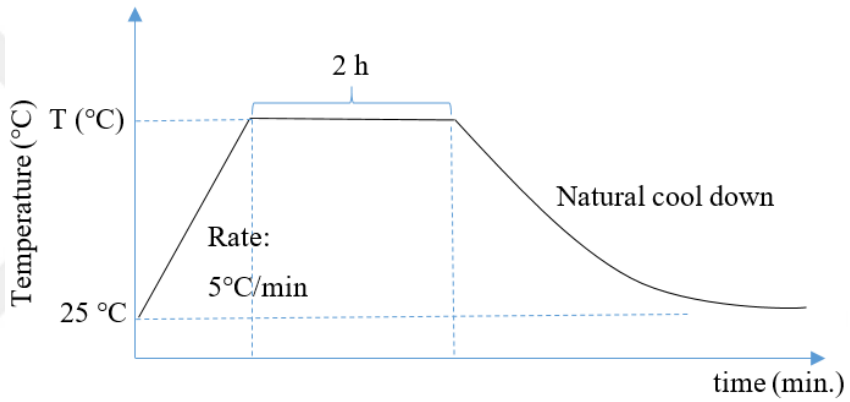

Figure 3.8. Schematic diagram of annealing procedure for T = 100, 200, 300 and 400 ˚C

3.2.3. Thermal Evaporation

After the thin films are deposited on ITO /SLG samples, which is electrically conductive but at the same time ionically blocking surface, they become ready for the thermal evaporation process. Aim of the thermal evaporation procedure is to create different diameter size contact areas for the electrical measurement, which is actually AC electrochemical impedance spectroscopy measurements. For this reason, top side of the films are covered with Aluminum by thermal evaporation technique to form capacitor like structure for the AC impedance spectroscopy measurements. During the evaporation process, mask with different diameter size openings are used to determine contact size dependence conductivity. Aluminum contact material is chosen for the top contact, since

it is also one of the chemical compounds (Al_2O_3) that is used during deposition. By this selection, it is also thought that no other contamination can be included. So, thermal evaporation is used for this purpose. First, the thin film samples are placed on the mask which is located at sample holder. Then, Aluminum metal (99.99 % purity) is cut into pieces and placed into Tungsten (W) boat for current to be applied. Before we put power on the boat to heat up, chamber of the thermal evaporator is evacuated firstly by a rough pump. Secondly, if the pressure has dropped to 10^{-2} millitorr, turbo molecular pump is turned on. After a while, the optimum vacuum pressure is reached for Al to be evaporated. So, the current output for resistive heating is turned on and set to approximately 112 Ampere. Melting point of aluminum is so low compared to the tungsten metal that we can eliminate its precipitation to the evaporated Aluminum gas, as it can stay in solid from while Al is evaporating. That's why Tungsten is chosen most of the time as crucible boat. Meanwhile, thickness of the Al contact is determined by the thickness sensor. Finally, Al contacts with 100 nm thickness will be evaporated on thin films for the electrical characterizations can be done.

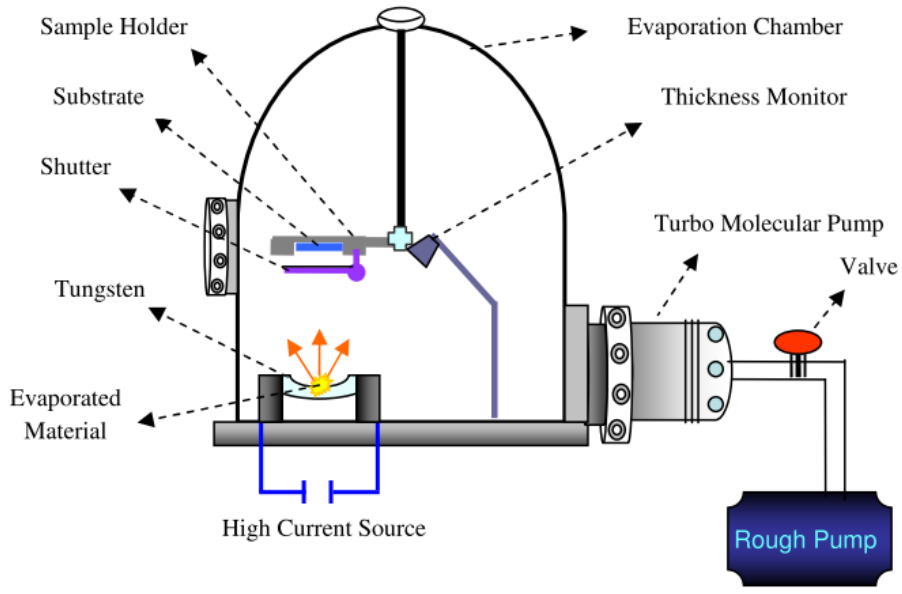

Figure 3.9. Schematic representation of thermal evaporation setup (Demirhan 2011).

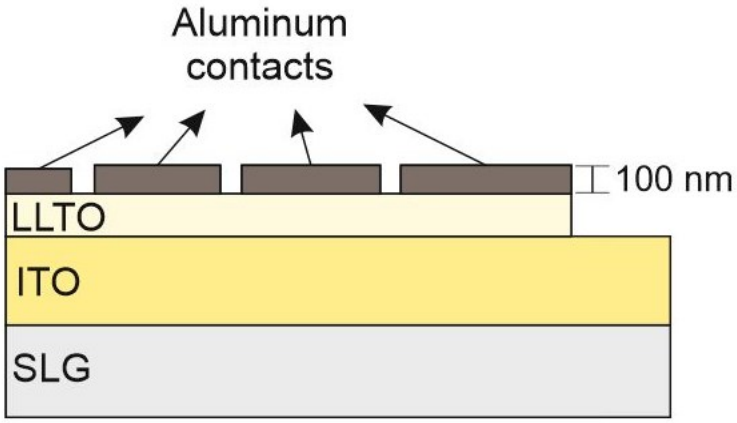

Figure 3.10. Cross-sectional view of the sample after Aluminum evaporation

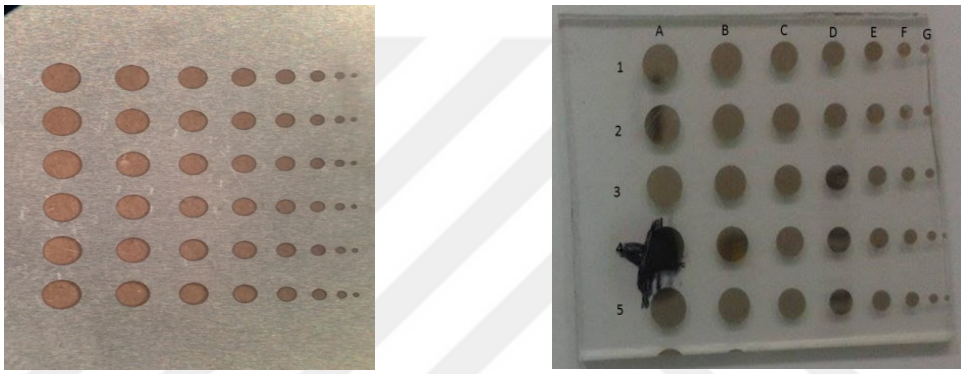

(a) (b)

Figure 3.11. Top view of the mask (a) and LLTO thin film sample after Aluminum is evaporated (b)

3.3. Characterization of the Targets and the Thin Films

3.3.1. Structural and Morphological Analysis

Prepared target compositions and each thin film deposited by RF magnetron sputtering were investigated. For the powder targets, X- ray powder diffraction is used to characterize the crystalline structure. So, the crystallinity of the targets with various compositions were determined by X-ray diffraction method using Philips X'Pert Pro X-ray diffractometer with Cu K_α X-ray radiation (λ= 1.5418 Å) over the angular range $20° < 2\theta < 80°$ with a scan rate of 0.139° /s. Crystallinity of the powders was checked by investigating the diffractograms. Furthermore, confocal Raman spectroscopy setup (Scientific Instruments) with Argon laser having 488 nm excitation wavelength with 600

grating is used to determine the vibrational peaks of $Li_{0.5}La_{0.5}TiO_3$ and $Li_{0.5}La_{0.5}Ti_{1-x}Al_xO_3$ targets with various x content.

For the thin film samples, crystallinity of the films cannot be detected by the X-ray powder diffractometer, since the thicknesses are too thin about 80-120 nm thicknesses which cannot be detected by this diffractometer. Also, confocal Raman spectroscopy setup was tried to focus on the sample. However, vibrational peaks of the substrate dominated results and only SLG substrate peaks were observed. So, Raman spectroscopy also have become useless for the structural investigation of the thin films. Therefore, morphological approach is needed in order to observe grain size distributions and grain boundaries. For this purpose, scanning electron microscopy is used for the thin films' morphological investigation. The surface morphology of the thin films with various Al_2O_3 content was examined by scanning electron microscopy (SEM) using Philips XL 30SFEG operated at 3.0 kV using TLD detector. Composition of the thin films cannot be controlled with EDS (energy dispersive spectroscopy) unit of the SEM, as the Li cannot be detected because of its low energy radiation. Also, another problem arises due to the low thickness of the thin films, which causes electron beam to penetrate through the thin film easily and access the underlying ITO electrode material. Therefore, it is not possible to get quantitative information using EDS.

For further investigation of the thin films, X-ray photoelectron spectroscopy was performed using a SPECS Phoibos 150 3D-DLD system with using Mg K_α radiation ($h\upsilon$ = 1254 eV) operated at 200 W, 1.5 kV. The pressure inside analysis chamber was always between 10^{-10}- 10^{-9} Torr. The high resolution scans of each element in $Li_{0.5}La_{0.5}Ti_{1-x}Al_xO_3$ were conducted at a 30 eV pass energy with a scan rate of 0.1 eV/s and the dwell time of 1s. The spectra were calibrated with respect to C 1s at 284.6 eV which is the characteristic of aromatic/aliphatic carbons. So, elemental constituents of the thin films were observable.

3.3.2. Electrical Characterization of the Thin Films

Impedance spectroscopy measurements were done by using IM 3590 HIOKI chemical impedance analyzer. Metal-Insulator-Metal structure was formed in order to measure the electrical properties of the LLTO thin films. The bottom electrode material is indium tin oxide (ITO) layer on soda-lime glass (SLG) substrate. During the sputtering

process one part of the ITO electrode layer is covered with an Aluminum foil to take contact from the back side preventing it be covered. Later, back contact ITO surface is covered with silver (Ag) paste to enhance its conductivity and prevent ohmic losses that arise from contacts materials. For the top metal contact, Aluminum (Al) is evaporated. Figure 3.12.(b) shows the capacitor like structure of the sample which is prepared for the impedance spectroscopy measurements.

Probe station is used to take contacts from ITO on the back side and Al on the top for AC Impedance spectroscopy measurements can be seen from the Figure 3.12. (a). AC Impedance spectroscopy measurements were conducted to evaluate ionic conductivity of $Li_{0.5}La_{0.5}Ti_{1-x}Al_xO_3$ thin films at room temperature within the frequency range from 0.1 Hz to 200 kHz.

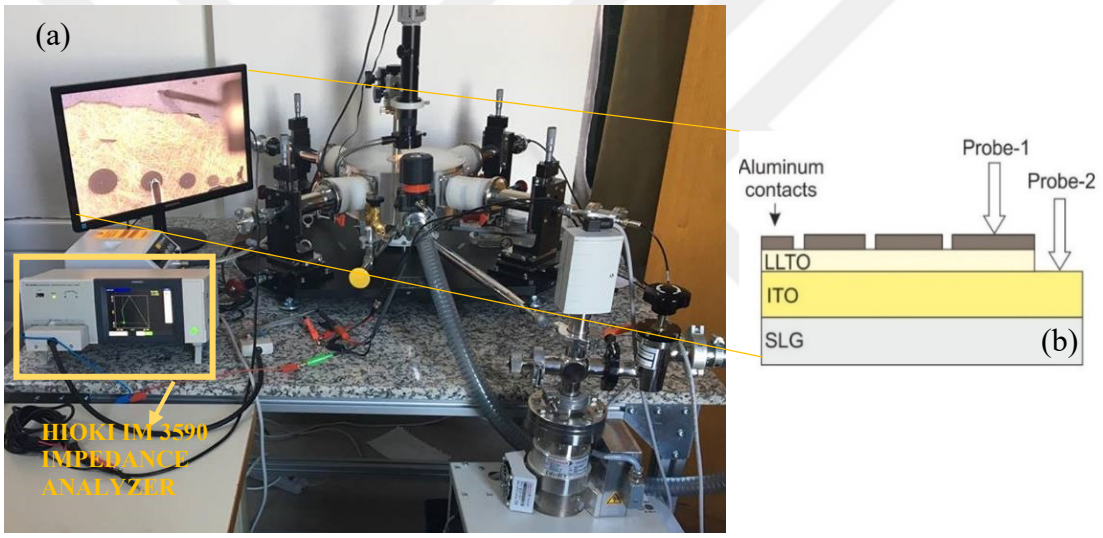

Figure 3.12. AC impedance spectroscopy measurement setup with probe station and monitor showing probes on the sample from (a) top view and (b) cross-sectional view of the sample.

Temperature dependent conductivity measurements are also examined by the Lakeshore temperature controller connected to probe station sample stage. Before the sample is placed on stage, DuPont is used to fix the sample on the stage and enhance thermal conductivity of the sample to have the same temperature with the temperature controller. Probe stage is then evacuated by turbo molecular pump equipment in order to provide thermal isolation of the setup from outside.

CHAPTER 4

RESULTS AND DISCUSSION

4.1. Characterization of the $Li_{0.5}La_{0.5}Ti_{1-X}Al_xO_3$ Targets Prepared by Conventional Solid State Reactions

Targets prepared after some steps of conventional solid state reactions, were characterized by X- ray powder diffraction and confocal Raman spectroscopy in order to obtain information about the crystalline structure and investigate vibrational mode changes according to Aluminum content (x) inside the $Li_{0.5}La_{0.5}Ti_{1-x}Al_xO_3$ (LLTAlO) powder compositions.

4.1.1. X-ray Powder Diffraction Analysis

For the crystallographic characterization of the targets X-ray powder diffraction (XRD) analysis were done to determine peaks for the planes of the perovskite LLTO structure. In Figure 4.1., all the diffraction peaks of the targets, at 2θ = 29.30º, 32.80º, 40.30º, 47.00º, 58.40º, 68.60º and 78.10º correspond to planes (101), (110), (112), (200), (212), (220) and (310) and can be ascribed to the reflections of $Li_{0.5}La_{0.5}TiO_3$ crystalline, which confirms that the fabricating process conducted in this work is appropriate with those reported in related literature results

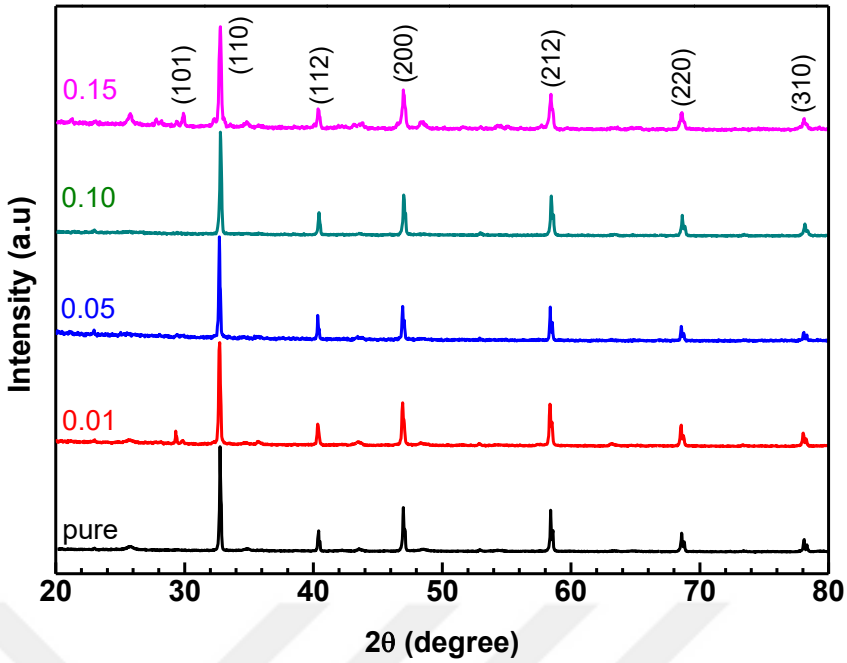

Figure 4.1. XRD patterns of all $Li_{0.5}La_{0.5}Ti_{1-x}Al_xO_3$ targets, which are expressed as nominal compositions of $Li_{0.5}La_{0.5}TiO_3$ (pure), $Li_{0.5}La_{0.5}Ti_{1-x}Al_xO_3$ (x=0.01, 0.05, 0.10, 0.15)

Although the mechanism and origin of the transport properties are interesting, they depend on the exact determination of the atomic arrangement in this material. Moreover, the actual crystal structure is still controversial because the stoichiometry, thermal stability, and crystal chemistry are not well established yet.

In spite of intense experimental work, the crystal structure of this system is still a matter of controversy. Structure of $Li_{0.5}La_{0.5}Ti_{1-x}Al_xO_3$ drifting of perovskite structure is mostly because of vacancies varying up to composition and can be changed by the heat treatments.

4.1.2. Raman Spectroscopy

Confocal Raman spectroscopy setup with Argon laser having 488 nm excitation wavelength with 600 grating is used to determine the vibrational peaks of $Li_{0.5}La_{0.5}TiO_3$ and $Li_{0.5}La_{0.5}Ti_{1-x}Al_xO_3$ targets with various x contents. It can be said that particular attention was paid to search and find a correlation between Raman parameters and Aluminum substitution. Attribution of modes could not be done precisely because spectra profile obtained is complex.

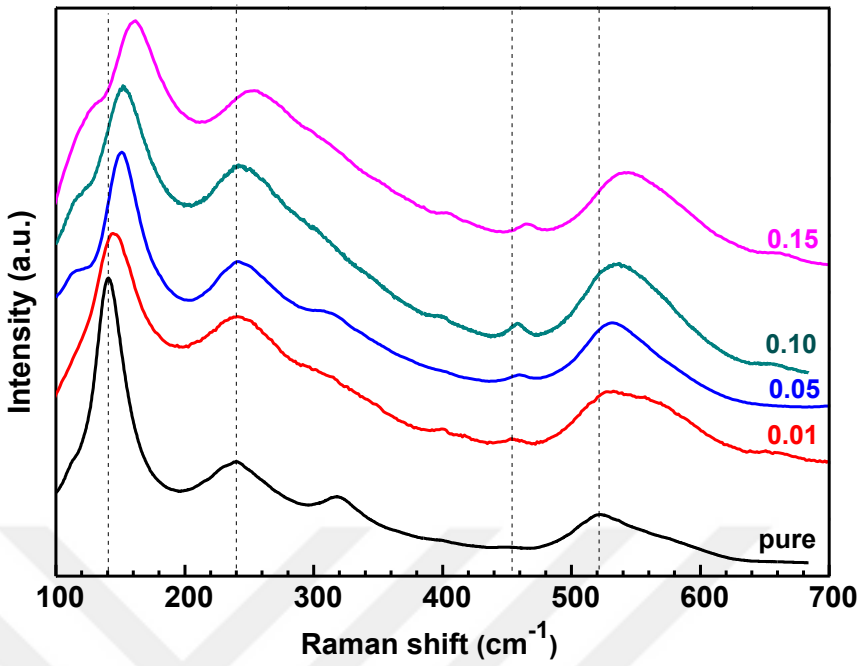

Figure 4.2. Raman spectroscopy results of the targets with different Al (x) compositions

In Figure 4.2, obtained Raman spectra with 4 vibrational mode peaks for different $Li_{0.5}La_{0.5}Ti_{1-x}Al_xO_3$ (x=0.00, 0.01, 0.05, 0.10, 0.15) compositions were presented. From this spectra vibrational modes of Ti and O_3 atoms can be examined, although there are also other elements such as Li, La and Al inside the chemical composition of powder targets. They don't give any vibrational mode peaks explicitly. However, their contribution and effects on bonding with Ti and O atom will affect the vibrational modes of Ti and O_3 peaks. Especially, amount of Aluminum substitution will affect the modes of Titanium.

So, for $Li_{0.5}La_{0.5}TiO_3$ (x = 0.00 (pure)) composition, four significant peaks located at 141.13, 239.84, 319.40, 522.64 cm^{-1} can be determined. These peaks belong to the vibrational modes of LLTO which corresponds to the vibrational modes of Ti (in plane), O3 in-plane, Ti (c-axis) and O (3) in-plane respectively. There is also very low intensity peak located at 460.15 cm^{-1} that can be attributed to O (1, 2) c-axis vibrational modes (Laguna et al. 2002)

For x = 0.01, it is observed three well defined peaks located at 145.27, 242.30, 532.21 cm^{-1} similar to x = 0.00 ($Li_{0.5}La_{0.5}TiO_3$) powder sample peaks. However, there exist peak shifts by Al substitution with Ti. In this sample, we do not have a peak signal from the peak at 319.40 cm^{-1} as in the previous case, which is ascribed to Ti (c-axis)

vibration mode. So, it can be referred that reduction of Ti ions inside will have caused 319.40 cm^{-1} peak to disappear.

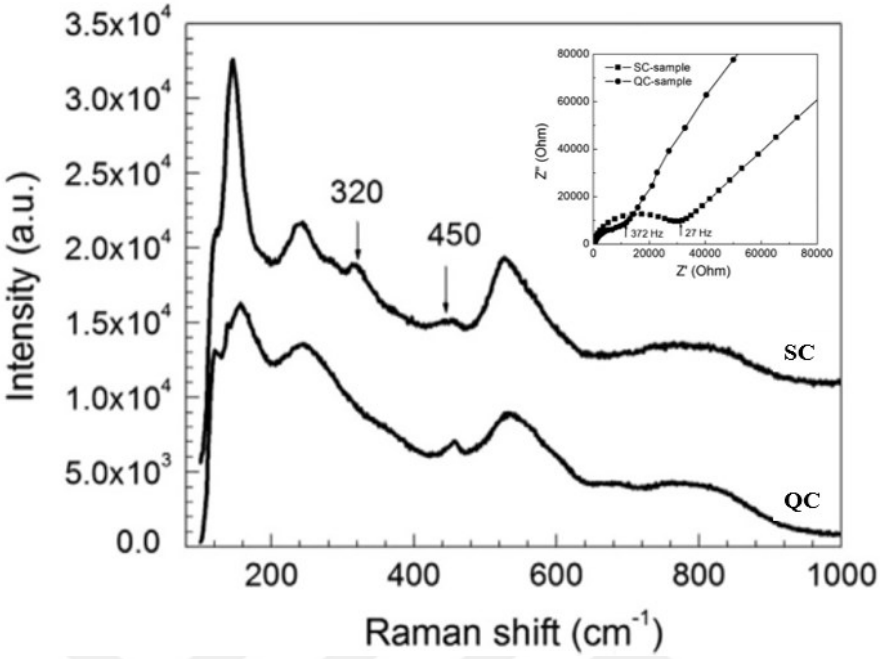

Figure 4.3. Raman spectra of slowly cooled (SC) and quickly cooled (QC) LLTO. The inset shows complex impedance plot of the same SC and QC samples. (Source: Trong, Thao, and Dinh 2015)

So, generally for other x = 0.05, 0.10, 0.15 compositions, same peak intensities are obtained but they are shifted compared to LLTO (pure) composition peaks. Moreover, the peak around 315 cm^{-1} for the pure LLTO composition shows strong depletion for Al included compositions which aims to substitute Al with Ti atom in the structure. The reason for the depletion of the peak at 315 cm^{-1} can be explained by the distortion of ABO_3 type perovskite structure as mentioned in (Trong, Thao, and Dinh 2015). In the study of Trong *et. al*., slowly and quickly cooled LLTO powder samples were investigated. In Figure 4.3., it is observed that the loss of peak intensity around 320 cm^{-1} is related with the distorted structure as it is a common result of quickly cooled samples. Also, the inset in Figure 4.3., which belongs to same samples shows the complex impedance spectra of QC and SC samples. It indicates QC samples that has more distortion compared to SC, is giving higher ionic conductivity result. So, the proposed idea for the similarity in between those peak distortion has a similar result with our study.

Table 4.1. Observed modes and attributions for different x- compositions of powder target samples (Omanda et al. 2014)

pure	x = 0.01	x = 0.05	x = 0.10	x = 0.15	Vibration modes
141.13 cm^{-1}	145.27 cm^{-1}	149.80 cm^{-1}	152.65 cm^{-1}	161.44 cm^{-1}	Ti (in-plane)
239.84 cm^{-1}	242.30 cm^{-1}	242.37 cm^{-1}	244.37 cm^{-1}	252.55 cm^{-1}	O (3) in-plane
319.40 cm^{-1}	-	312.80 cm^{-1}	-	-	Ti (c-axis)
460.15 cm^{-1}	454.59 cm^{-1}	460.02 cm^{-1}	458.86 cm^{-1}	466.23 cm^{-1}	O (1,2) c-axis
522.64 cm^{-1}	532.21 cm^{-1}	530.53 cm^{-1}	535.44 cm^{-1}	542.17 cm^{-1}	O (3) in-plane

Furthermore, from Table 4.1, investigation of in-plane oxygen vibrations can be done. The peak intensity around 230 cm^{-1} would be due to O-Ti-O bond bending and the other in-plane oxygen vibration belong to Ti-O bond stretching can be ascribed to the peak intensity around 525 cm^{-1}. It is also observed that peak intensities around 144 cm^{-1} show a decrease by the reduction in Ti amount for x = 0.01, 0.05, 0.10, 0.15 compositions. The decrease in peak intensities of Ti is not remarkable, since the amount of reduction is so less that it will not show an enormous effect on the peak intensities.

The most obvious result in Al substitution with Ti, is the peak shift by the substitution. The reason behind those peak shifts in vibrational modes can be explained by the analogy to simple harmonic motion. So, when the simple harmonic motion relation is solved for the angular frequency, ω:

$$F = -k.x = m.a = m.\frac{d^2x}{dt^2} = m.\ddot{x} \tag{4.1}$$

And the path (x) during the simple harmonic motion can be expressed as;

$$x = A_o.\sin(\omega t + \varphi) \tag{4.2}$$

$$\dot{x} = A_o.\omega.\cos(\omega t + \varphi) \tag{4.3}$$

$$\ddot{x} = -A_o.\omega^2.\sin(\omega t + \varphi) = -x.\omega^2 \tag{4.4}$$

So, the angular frequency that corresponds to vibrational frequency (ω) is;

$$F = -k.x = m.\ddot{x} = -m.x.\omega^2 \tag{4.5}$$

$$\omega = \sqrt{\frac{k}{m}} \tag{4.6}$$

where k is the spring constant that corresponds to bonding energies and m is the mass of the constituents (DeHoff 2006). The difference in mass of Ti substituted with Al and changes in bonding cause vibrational frequency to shift. So, it is understood from the Eqn.(4.6) that not only the bonding has an effect on vibrational frequency, but also change in mass will have an effect on vibrational modes.

To sum up, the spectrum basically consists of four bands. The bands at 140 and 320 cm^{-1} are ascribed to modes involving in plane and c-axis titanium vibration, respectively, while the bands at 239 and 521 cm^{-1} are assigned to oxygen (Antoniassi et al. 2011). Al_2O_3 addition caused peaks to shift left from the pure LLTO peak, which proves that the increasing amount of Al in thin film composition, shifts the peaks. This is because vibrations from Ti and O bonding has changed by the substitution. B-O distance is decreased while A-O distance is increasing as it is explained in the study of Morata-Orrantia et al. (Morata-Orrantia, Garcıa-Martin, and Alario-Franco 2003) that this situation in the crystal structure gives support to Li-ion motion (Omanda et al. 2014).

Besides, it should be noted that those Raman analyses above are done on powder target samples. It is also tried to be obtained Raman analysis for the thin film compositions. Laser of the Raman setup that has 488 and 514 nm wavelength options are tried to be focused on thin film samples, whose thicknesses are about 80-120 nm. Since the thin film thicknesses are too far away to dominate the vibrational modes coming from the SLG substrate, it is not possible to get Raman data of the thin film samples. Although the thin film sample with the highest thickness, which is about 120 nm, is examined, vibrational modes of the sample cannot be detected.

4.2. Characterization of the $Li_{0.5}La_{0.5}Ti_{1-x}Al_xO_3$ Thin Films

4.2.1. X-ray Diffraction

For the thin film samples that were grown on ITO/SLG substrate are tried to be observed by the X-ray powder diffractometer in the Material Research Center of the Izmir Institute of Technology. However, X-ray detector shows the peaks of the substrates, which can be the reason that the films are not showing crystalline property. So, the thin films can be assumed to be amorphous but this is not a clear issue yet because the SEM images of those films showing grain like structures. Here, it can be proposed that the thicknesses of the films are so small that crystallinity cannot be detected by X-ray powder diffraction. Therefore, as it can be seen from the Figure 4.4. that crystalline peaks of ITO are dominant, since the penetration depth is higher in that device.

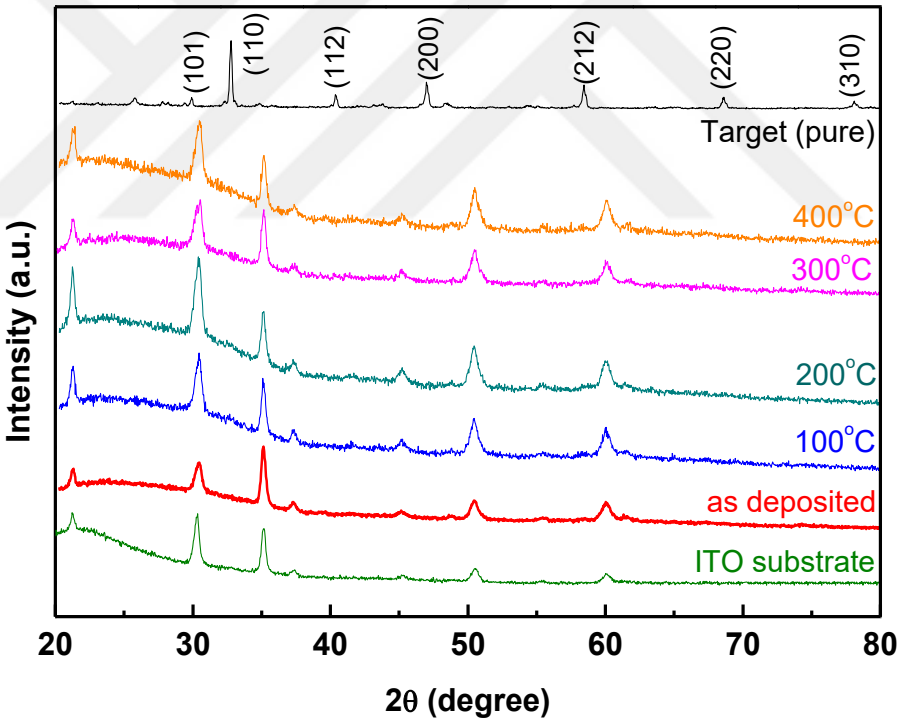

Figure 4.4. XRD patterns of $Li_{0.5}La_{0.5}TiO_3$ (pure) target and films according to that targets with anneal treatments in air for 2 h at 100, 200, 300 and 400 °C and the crystalline peaks of the ITO substrate.

So, from Figure 4.4., it can be observed that all grown thin film samples on ITO substrate do not show any overlapping peaks with crystalline powder target. As deposited and annealed thin films at 100, 200, 300, 400 °C according to $Li_{0.5}La_{0.5}TiO_3$ (pure)

composition are examined. Aim of the anneal treatment is to investigate any crystallization caused by the annealing procedure. Although it is expected to observe crystallization by the increase in annealing temperature, XRD results do not show any peaks inaccordance with the LLTO target, which is sputtered on ITO substrates as thin films with 100 nm thickness. Moreover, further anneal treatments above 400 °C is avoided, as it may result in ITO substrate diffusion toward LLTO thin film sample.

To conclude, peaks appear from thin film samples are only the peaks of ITO substrate that prevents us to decide on thin film structure. If there will be an opportunity to analyze thin film sample of LLTO with the grazing incidence XRD, instead of a powder diffraction device., it would be better choice to understand the structure of thin films.

4.2.2. Scanning Electron Microscopy (SEM)

Scanning electron microscopy is used to investigate the surface morphology of the thin film samples. General outlook of the structures can be observed with this technique. Its operational principle is similar in some sense to the conventional light microscope but the light is replaced with the electrons. The resolution, magnification and the depth of field are based on the same properties but the technology between the light microscope and the electron microscope is different because of the different nature of light and electrons. In conventional light microscope, light that is in the visible region of the spectrum, can be detected by the human's eye and it has some limitations for magnification with higher resolution. The lowest particle size limit in the traditional microscope is about 1 μm, but in the scanning electron microscopy, the resolution is only few (< 5) nanometers depending on the hardware and operating conditions (Linnala 1990). Scanning electron microscopy accelerates the electron for the scan, which will cause electron to gain velocity and as a consequence of wave nature of moving electrons, smaller wavelengths of photon can scan the structure in lower dimensions which can be theoretically calculated frım the de Broglie wavelength relation from the Eqn.(4.7) (Beiser 2003). So, by this technology, higher resolutions can be achieved.

$$\lambda = \frac{h}{p} = \frac{h}{m\vartheta} \tag{4.7}$$

Besides, SEM has some requirements on the sample type and sample preparation. The sample has to be clean and dry, it can't be volatile or include dissolved gas which could be released into the chamber. The conductivity of the sample is another important issue that should be considered because a nonconductive material causes charging which weakens the quality of the image. That is why the samples must be coated with a thin layer of carbon, gold or gold-palladium for most of the time if it is required. However, it should be first tried to take the image without any metallic coverage, as it will also effect the structure of the sample that we want to investigate. Therefore, another method is tried. The stage of the sample and the sample surface, which is nonconductive layer is bonded with a metallic tape to its holder for SEM analysis of LLTO thin films. So, it will help to reduce charging effect caused by the nonconductive layer of the sample.

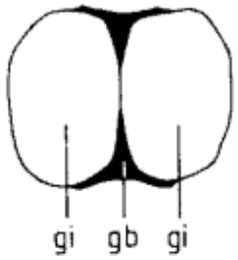

Figure 4.5. Schematic representation of the two adjacent grains and the grain boundary between them (Source: Barsoukov and Macdonald 2005)

In our experimental study, it is important to examine grain structure, size, connections and boundaries to explain ionic conduction behavior of the samples, since the conduction differ according to medium that the ion is interaction when passing through. For instance, as it can be seen from the Figure 4.5, an ion passing from one grain to another grain will experience different diffusion conditions that will result in different conductivity values.

4.2.2.1. Surface Morphology of Different $Li_{0.5}La_{0.5}Ti_{1-X}Al_xO_3$ Thin Film Compositions

Thin film samples that are grown on ITO/ SLG substrates with different $Li_{0.5}La_{0.5}Ti_{1-x}Al_xO_3$ compositions can be compared by SEM images in Figure 4.6.

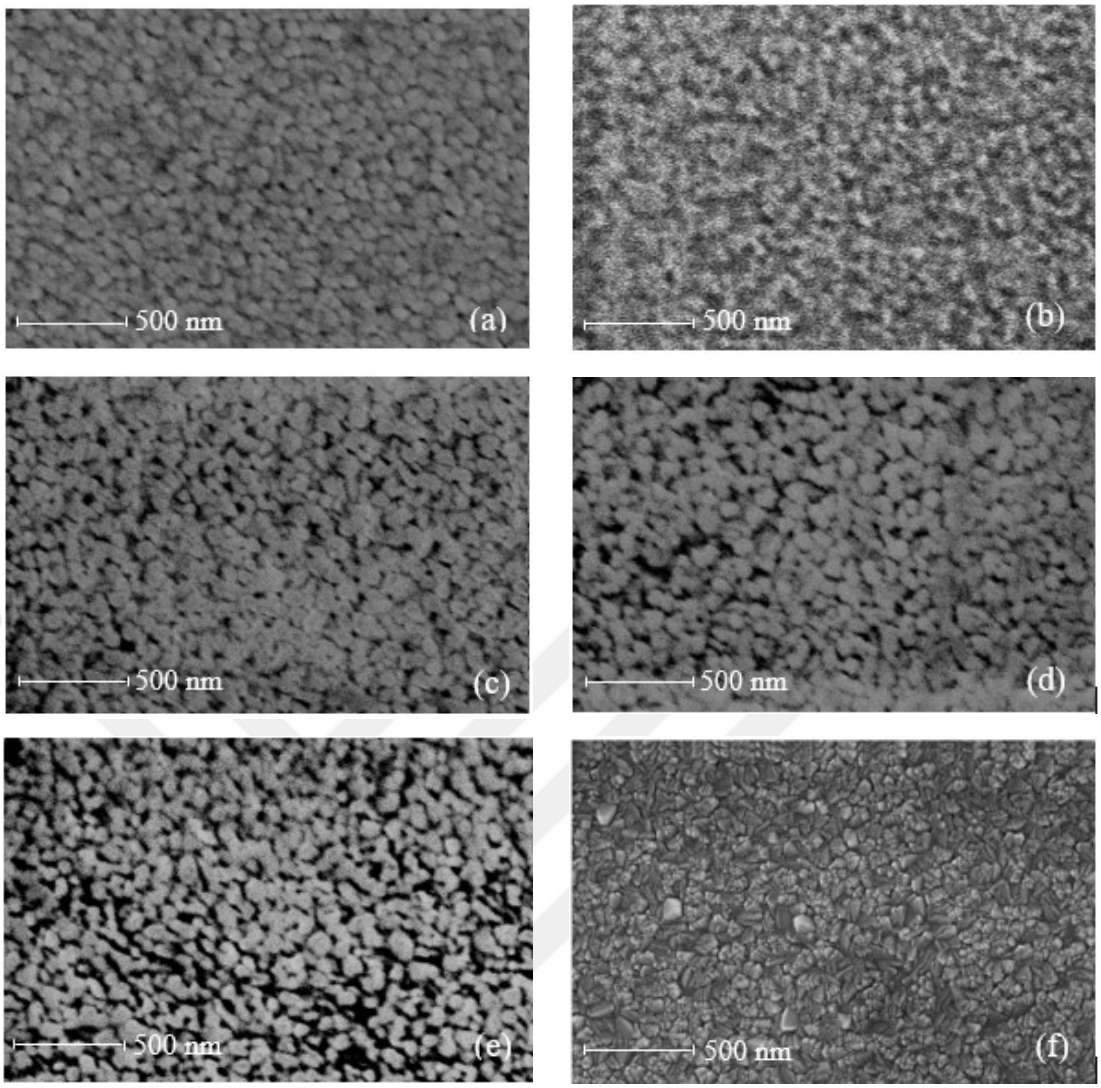

Figure 4.6. SEM image of the surface of (a) $Li_{0.5}La_{0.5}TiO_3$ thin film without Al_2O_3 addition (b) thin film obtained from $Li_{0.5}La_{0.5}Ti_{1-x}Al_xO_3$ (x=0.01) (c) from $Li_{0.5}La_{0.5}Ti_{1-x}Al_xO_3$ (x=0.05) (d) $Li_{0.5}La_{0.5}Ti_{1-x}Al_xO_3$ (x=0.10) (e) $Li_{0.5}La_{0.5}Ti_{1-x}Al_xO_3$ (x=0.15) targets deposited by RF magnetron sputtering on ITO/SLG substrates and the SEM image of (f) ITO substrate.

Table 4.2. Grain size averages of different $Li_{0.5}La_{0.5}Ti_{1-x}Al_xO_3$ compositions of pure (x = 0.00), x = 0.01, x = 0.05, x = 0.10, and x = 0.15.

	pure	**0.01**	**0.05**	**0.10**	**0.15**
Grain size average	51.8 nm	77.6 nm	59.2 nm	65.2 nm	65.6 nm

It can be observed from the Figure 4.6**.** that $Li_{0.5}La_{0.5}TiO_3$ (pure) thin films have smaller grain size that results in larger number of grain boundaries compared to LLTAlO (x = 0.01) and LLTAlO (x = 0.05) composition. For this reason, LLTAlO (x = 0.01) and

(x = 0.05) have higher ionic conductivities compared to LLTO (pure). It is expected that larger the grain boundary areas lower ionic conductivity.

Although it seems for LLTAlO (x = 0.10) case that there exist more grain boundaries compared to LLTO (pure), ionic conductivity results point out the effect of grain size. For LLTAlO (x = 0.10) grain size average is 65.24 nm, while for LLTO (pure) composition grain size average is equal to 51.81 nm. Moreover, it means also bigger the grain sizes, larger the number of the grain boundaries that an ion is facing through conduction. In Figure 4.6 (a), it is obvious that the grains of the x = 0.01 thin film composition has the highest connectivity compared to other compositions and it shows the highest ionic conductivity, which leads to build up a relation between grain connectivity and ionic conduction, if there is not an unknown parameter that effects the structure unconsciously (i.e., charging effect while taking the SEM image). However, beside the other compositions, SEM image for the LLTO (x = 0.15) shows larger grain boundary areas that corresponds to darker areas within the grain structures which is the reason for this chemical composition (x = 0.15) to have lowest ionic conductivity. Therefore, it is understood that there is a critical amount of Al addition to enhance ionic conductivity as it is supported by the impedance measurements.

In other words, it can be concluded that addition of Aluminum has a balance between grain size and grain boundary construction. But there is a limit in aluminum content for this balance to be valid, otherwise the structure will be too much distorted.

4.2.2.2. Effect of Anneal Temperature on Each Composition of $Li_{0.5}La_{0.5}Ti_{1-X}Al_xO_3$ Thin Films

Effect of anneal on every composition is examined separately in order to investigate any difference in the grain size and its connection between the impedance results of the thin film samples. SEM images with different scales can be found in the Table 4.3,4,5,6,7 to make comparison between the grain structures and sizes. First, SEM images of the thin film samples are taken. Then, grain sizes are determined by ‘Scandium’ program that can calculate the grain size from SEM images.

Table 4.3. SEM images of surfaces of as deposited $Li_{0.5}La_{0.5}TiO_3$ thin film and $Li_{0.5}La_{0.5}TiO_3$ thin films annealed at 100 ˚C, 200 ˚C, 300 ˚C, and 400 ˚C with 500 nm, 1µm scales and grain size average.

	Anneal temperature (˚C)	500 nm bar length	1 µm bar length	Grain size average
pure	as deposited	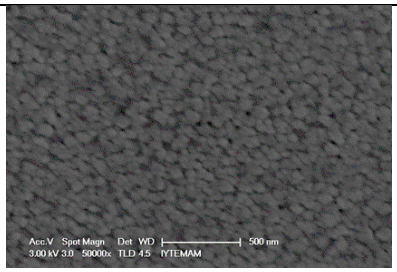	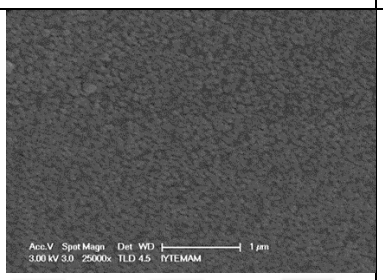	51.81 nm
	100 ˚C	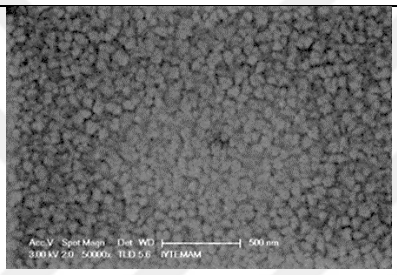	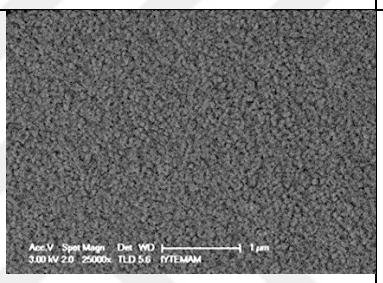	54.49 nm
	200 ˚C	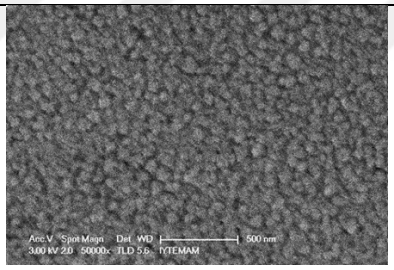	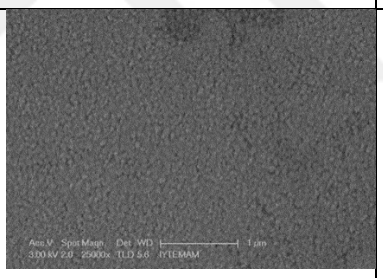	57.45 nm
	300 ˚C	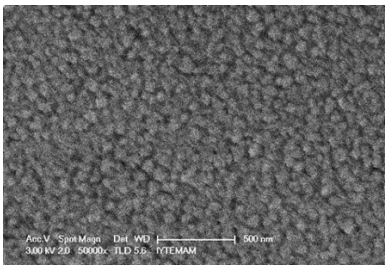	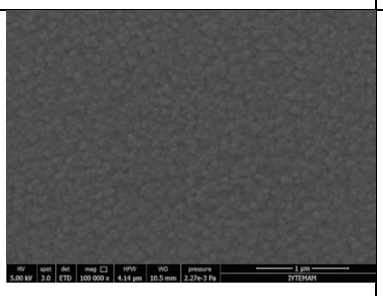	-
	400 ˚C	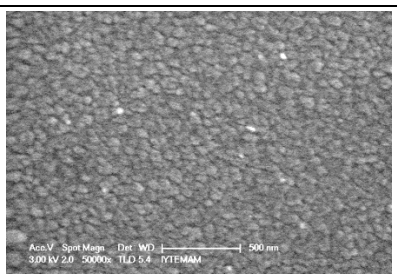	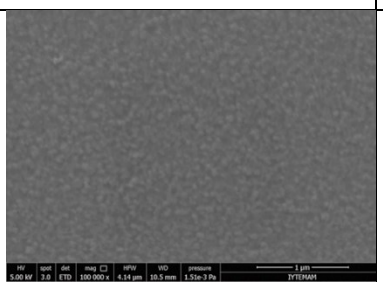	53.37 nm

Ionic conductivity results of $Li_{0.5}La_{0.5}TiO_3$ composition of the thin films can be ordered from higher to lower conductivities as; $\sigma_{300^\circ C} > \sigma_{400^\circ C} > \sigma_{300^\circ C} > \sigma_{as\ deposited} > \sigma_{100^\circ C} > \sigma_{200^\circ C}$.

From the view of ionic conductivity results, SEM images can be interpreted. Generally, increase in temperature causes grain sizes to increase as it allows diffusion of atoms from one side of the boundary to the other.

$Li_{0.5}La_{0.5}TiO_3$ thin film annealed at 300 ˚C has grain clusters that has formed larger grains. Therefore, it shows the highest ionic conduction among other annealing temperatures. For the $Li_{0.5}La_{0.5}TiO_3$ thin film sample annealed at 400 ˚C, it can be suggested that there are shiny, white dot like structures on the surface which can be the sign of diffusing ITO (Indium Tin Oxide) substrate at higher annealing temperatures (Koseoglu et al. 2015).

Table 4.4. SEM images of surfaces of as deposited $Li_{0.5}La_{0.5}Ti_{1-x}Al_xO_3$ (x=0.01) thin film and $Li_{0.5}La_{0.5}Ti_{0.99}Al_{0.01}O_3$ thin films annealed at 100 ˚C, 200 ˚C, 300 ˚C, and 400 ˚C with 1µm, 2/3µm scales and grain size average.

	Anneal temperature (˚C)	1 µm bar length	Grain size average
x = 0.01	**as deposited**	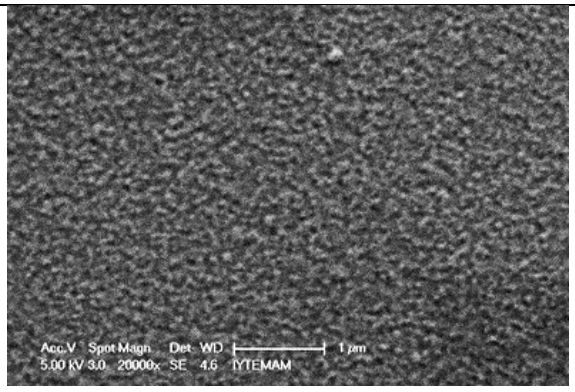	77.61 nm
	100 ˚C	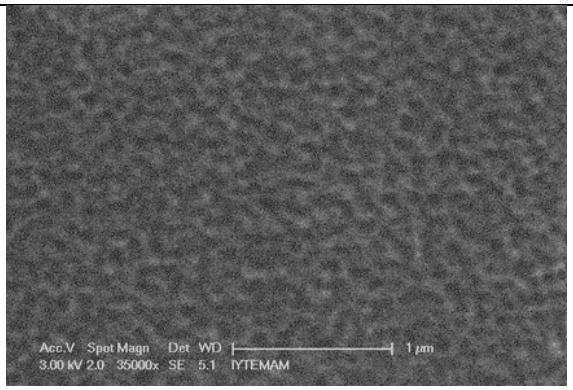	81.54 nm

(cont. on next page)

Table 4.4. (cont.)

	200 ˚C	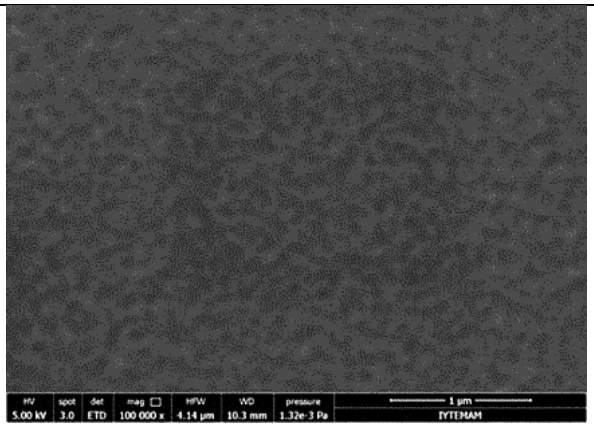	114.76 nm
	300 ˚C	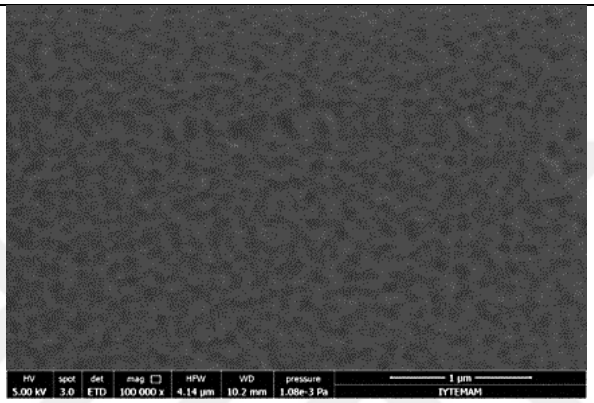	92.69 nm
	400 ˚C	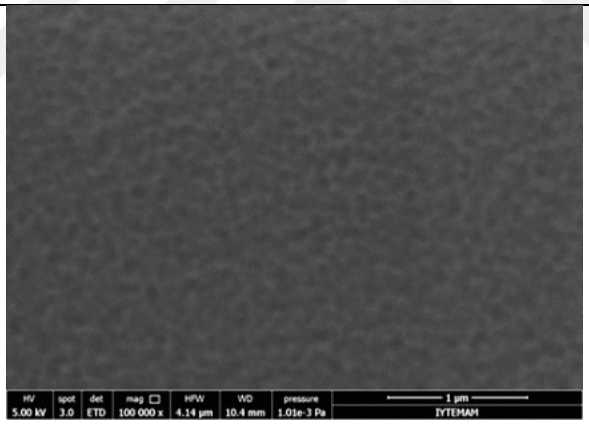	100.80 nm

For $Li_{0.5}La_{0.5}Ti_{0.99}Al_{0.01}O_3$ (x=0.01) thin film composition, anneal treatment do not show a trend-line by the increase in temperature. Ionic conductivity results from the impedance spectroscopy measurements can be arranged as follows : $\sigma_{100^{\circ}C} > \sigma_{as\ deposited} > \sigma_{300^{\circ}C} > \sigma_{200^{\circ}C} > \sigma_{400^{\circ}C}$.

So, it can be referred only that $Li_{0.5}La_{0.5}Ti_{0.99}Al_{0.01}O_3$ thin film sample annealed at 100 ˚C have clear difference from the other ones. Connectivity between the grains are so dense like a cloud and the grain boundary regions are smaller than the other anneal treatments conducted on $Li_{0.5}La_{0.5}Ti_{0.99}Al_{0.01}O_3$ composition.

Table 4.5. SEM images of surfaces of as deposited $Li_{0.5}La_{0.5}Ti_{1-x}Al_xO_3$ (x=0.05) thin film and $Li_{0.5}La_{0.5}Ti_{0.95}Al_{0.05}O_3$ thin films annealed at 100 ˚C, 200 ˚C, 300 ˚C, and 400 ˚C with 1μm scale and grain size average.

	Anneal temperature (˚C)	**1 μm bar length**	**Grain size average**
x = 0.05	**as deposited**	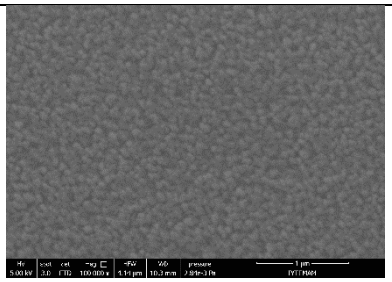	59.15 nm
	100 ˚C	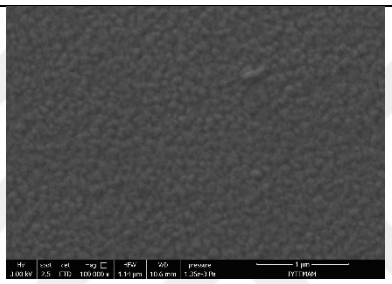	67.2 nm
	200 ˚C	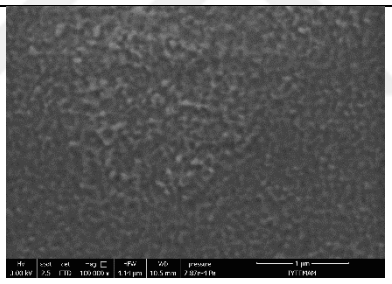	74.52 nm
	300 ˚C	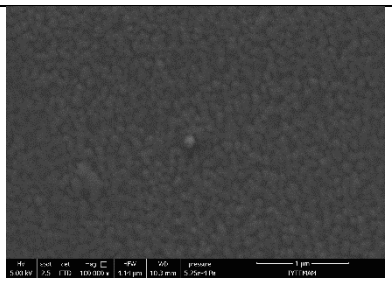	75.14 nm
	400 ˚C	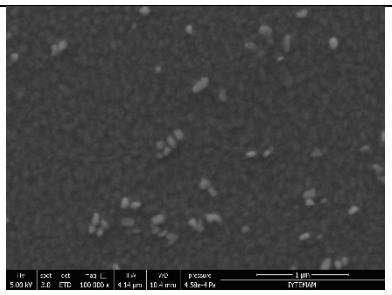	63.86 nm

SEM images of $Li_{0.5}La_{0.5}Ti_{1-x}Al_xO_3$ (x=0.05) thin films are tabulated above to understand the effect of anneal treatments. Similar to previous x=0.01 annealed at 100 ˚C, for $Li_{0.5}La_{0.5}Ti_{1-x}Al_xO_3$ (x=0.05) annealed at 200 ˚C image includes also ghost like structures referred as highly conducted grain communities that result in higher ionic conductivity. Again another similarity with the previous composition is that there are also different phases (white like color) appear on the surface that can be proposed as reason for the lower ionic conduction. The order of the conductivity results obtained from this annealing is like as follows; : $\sigma_{200^\circ C} > \sigma_{300^\circ C} > \sigma_{as\ deposited} > \sigma_{400^\circ C} > \sigma_{100^\circ C}$.

Table 4.6. SEM images of surfaces of as deposited $Li_{0.5}La_{0.5}Ti_{1-x}Al_xO_3$ (x=0.10) thin film and $Li_{0.5}La_{0.5}Ti_{0.90}Al_{0.10}O_3$ thin films annealed at 100 ˚C, 200 ˚C, 300 ˚C, and 400 ˚C with 1µm scale and grain size average.

	Anneal temperature (˚C)	**1 µm bar length**	**Grain size average**
x = 0.10	**as deposited**	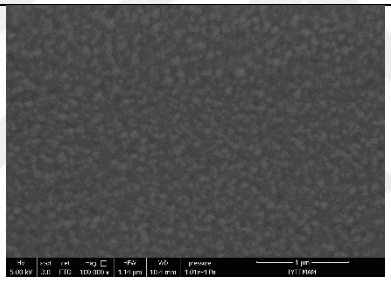	65.24 nm
	100 ˚C	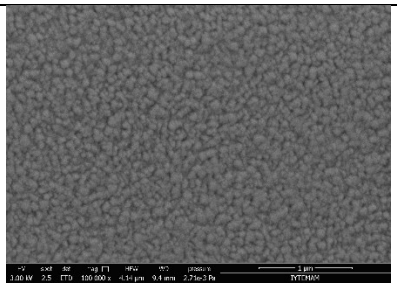	76.48 nm
	200 ˚C	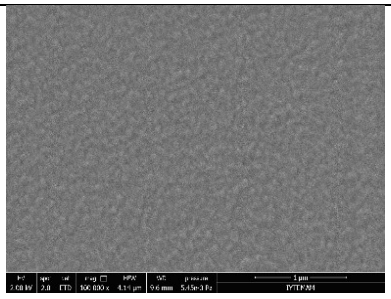	63.91 nm

(cont. on next page)

Table 4.6. (cont.)

	300 ˚C	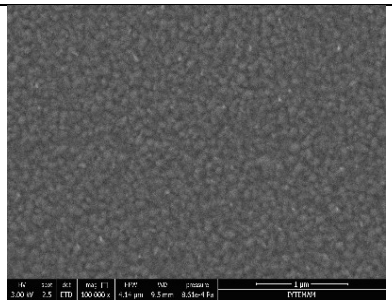	68.93 nm
	400 ˚C	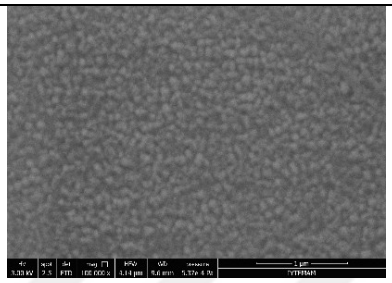	76.11 nm

Conductivity order of the SEM images above for thin film $Li_{0.5}La_{0.5}Ti_{1-x}Al_xO_3$ (x=0.10) composition; $\sigma_{400^\circ C} > \sigma_{100^\circ C} > \sigma_{as\ deposited} > \sigma_{300^\circ C} > \sigma_{200^\circ C}$. This time, it is unexpected to see the highest ionic conductivity value from 400 ˚C anneal treatment, as it always results in lower conductivity value because of the diffusion of ITO showing white dot like sign of it. However, there isn't any observable phase difference apparently. The grain size average for this temperature is 76.11 nm, which is the largest compared to lower heat treated ones.

Table 4.7. SEM images of surfaces of as deposited $Li_{0.5}La_{0.5}Ti_{1-x}Al_xO_3$ (x=0.15) thin film and $Li_{0.5}La_{0.5}Ti_{0.85}Al_{0.15}O_3$ thin films annealed at 100 ˚C, 200 ˚C, 300 ˚C, and 400 ˚C with 500 nm, 1µm scale and grain size average.

		500 nm bar length	**1 µm bar length**
x = 0.15	**as deposited**	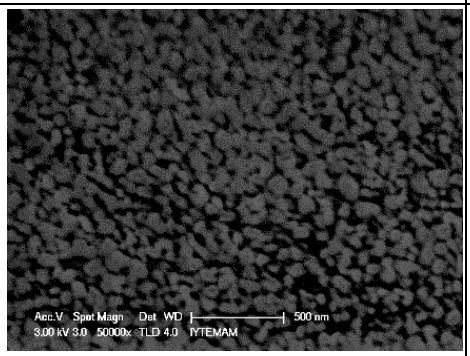	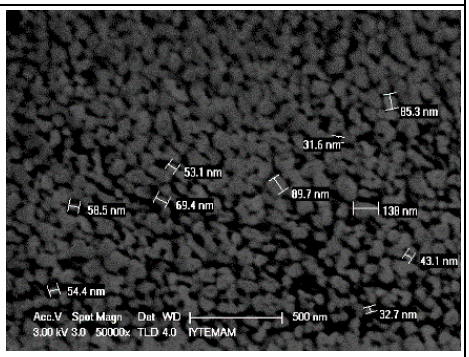
	Grain size average	65.58 nm	

In this case, after finding that the $Li_{0.5}La_{0.5}Ti_{1-x}Al_xO_3$ (x=0.15) composition does not promoting ionic conduction compared to pure one, it is not required to conduct annealing on the samples. So, the grain size for as deposited $Li_{0.5}La_{0.5}Ti_{0.85}Al_{0.15}O_3$ composition is calculated as 65.58 nm.

4.2.3. X-ray Photoelectron Spectroscopy

X-ray photoelectron spectroscopy (XPS) was used to characterize the chemical nature of $Li_{0.5}La_{0.5}Ti_{1-x}Al_xO_3$ thin films. In Figure 4.7., general survey of $Li_{0.5}La_{0.5}Ti_{1-x}Al_xO_3$ thin films with various Al (x) content, which are denoted by pure (x = 0.00), x = 0.05, x = 0.10 and x = 0.15 labels, are shown. The XPS spectra consists of peaks assigned to La 3d, La 4d, La 4p, La5p, Ti 2s, Ti 3s, Ti 3p, Ti 3d, O 1s, Al ? (Al 2s,120-116 eV, Al 2p 71-75 eV) and C 1s. The peak at 284.6 eV assigned to C 1s was used as a reference peak for the calibration (Chen et al. 2012). Peaks appear in the spectrum is the result of atoms emitting electrons of a particular characteristic energy.

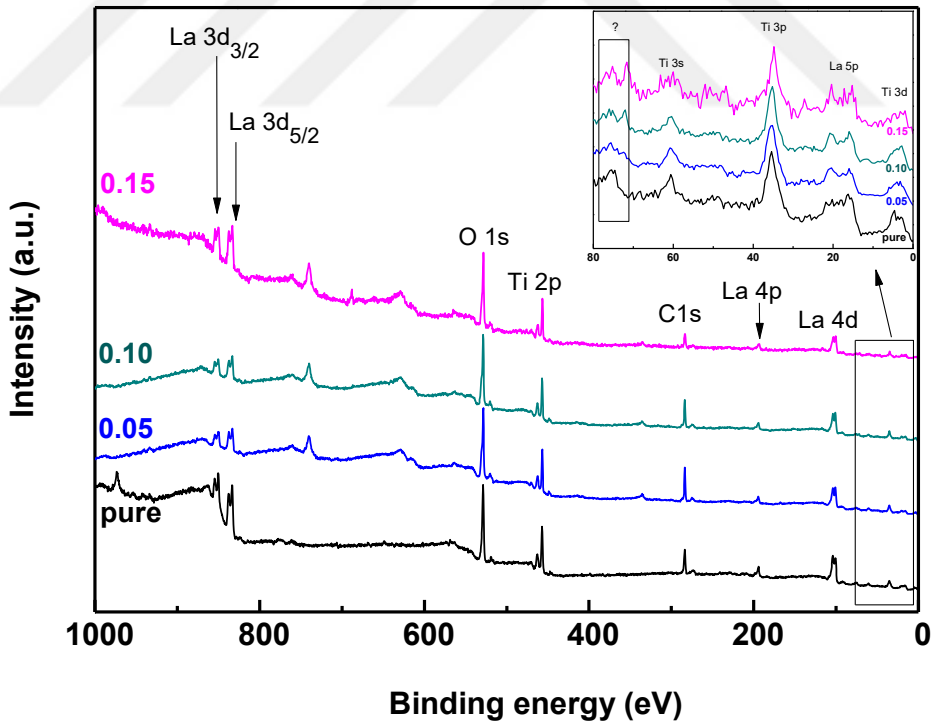

Figure 4.7 XPS spectra of $Li_{0.5}La_{0.5}TiO_3$ (pure) and $Li_{0.5}La_{0.5}Ti_{1-x}Al_xO_3$ for different x-compositions of x = 0.05, x = 0.10 and x = 0.15

The energies and intensities of the peaks in general XPS spectra were used to identify the surface elements and it is proved that thin film depositions are successful in

forming LLTO compositions. However, there is no significant peak for Li 1s which must be located in between 56-54 eV region. Therefore, dwell time should be increased in order to clarify Li 1s signal can be detected or not. For further information, detailed spectra analysis on La 3d, Ti 2p, Al 2p, O 1s regions were investigated. These peaks were useful to determine the oxidation states of the compounds (Pham, Bohnke, and Bohnke 2004).

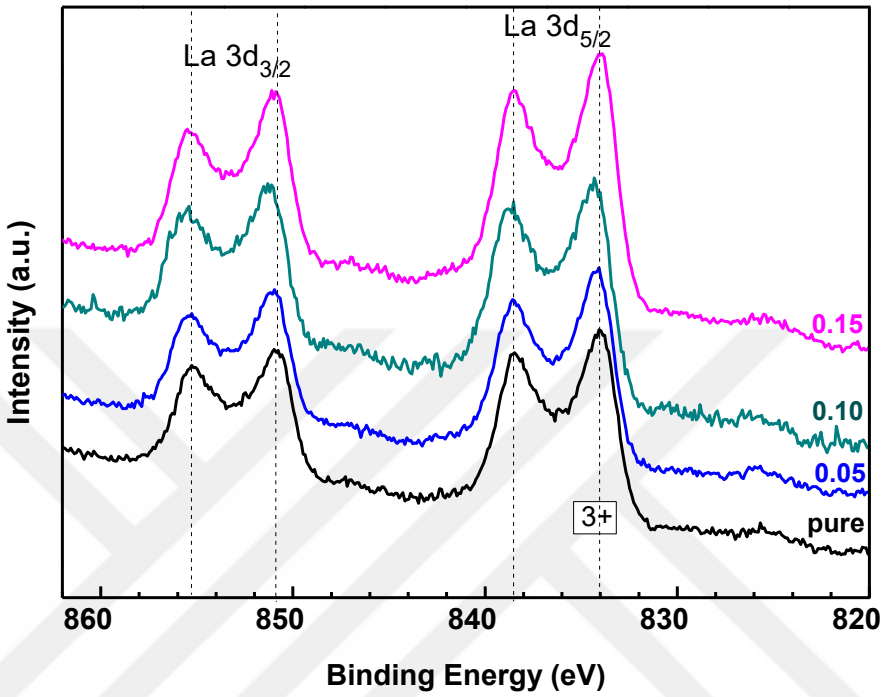

Figure 4.8 XPS spectra of $Li_{0.5}La_{0.5}Ti_{1-x}Al_xO_3$ thin films with various x-content labeled as pure, 0.05, 0.10 and 0.15 from La 3d region.

In Figure 4.8, La 3d region is shown for the different compositions of $Li_{0.5}La_{0.5}Ti_{1-x}Al_xO_3$. Here, only a slight variation in peak positions and intensities are observable. The peak at 834 eV assigned to La^{+3} state seems to be stable against Al substitution.

In Figure 4.9., there are two peaks for Ti 2p region, showing slight shift toward higher binding energies which can be interpreted as Ti-O bond shortening with Al substitution. Also, Ti $2p_{1/2}$ and Ti $2p_{3/2}$ peaks at 463.32 eV and 457.71 eV can be attributed to oxidation state of Ti^{+4} coordinated with O^{-2} ions like in TiO_2 structure (Li, Zhang, and Fu 2006). Besides, it is obvious that peak intensity of Ti $2p_{3/2}$ for x = 0.15 is low, as much of the Ti is replaced by Al which results in decrease in Ti peak intensity.

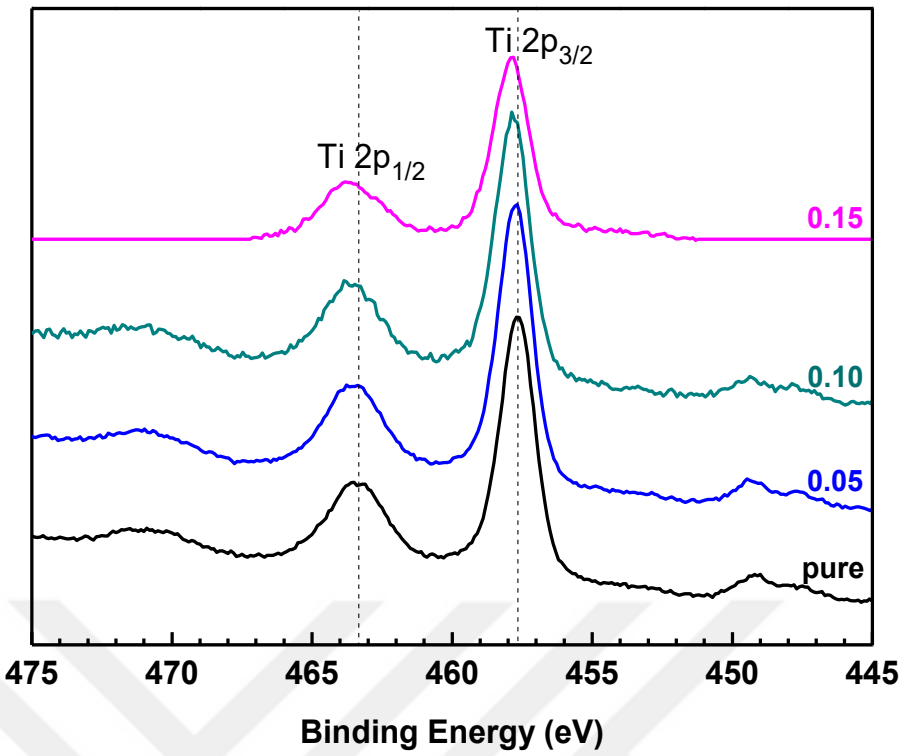

Figure 4.9. XPS spectra of $Li_{0.5}La_{0.5}Ti_{1-x}Al_xO_3$ thin films with various x-content labeled as pure, 0.05, 0.10 and 0.15 from Ti 2p region.

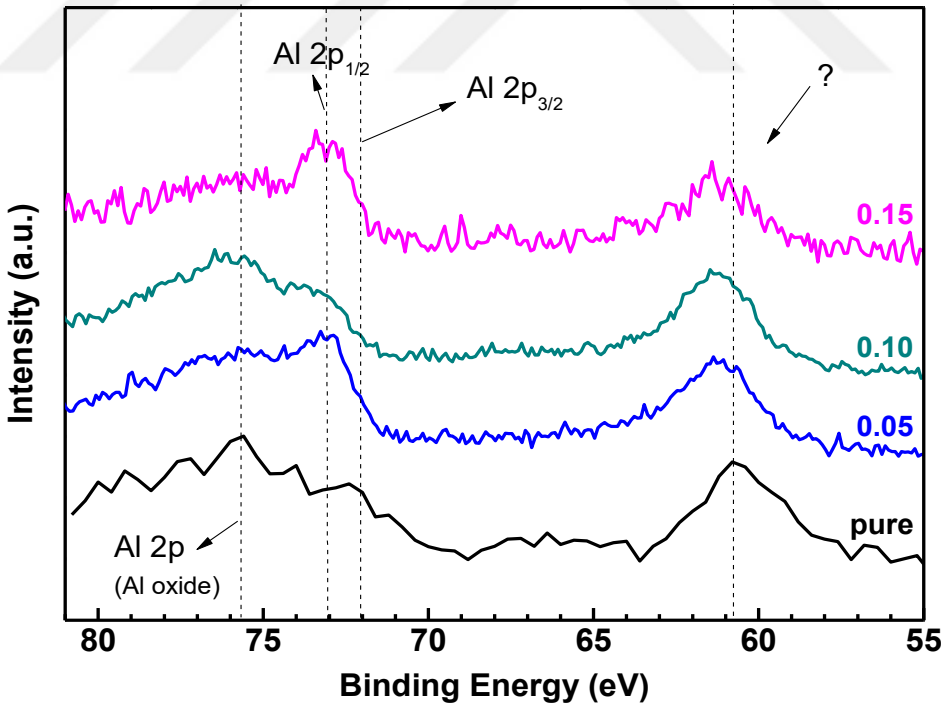

Figure 4.10 XPS spectra of $Li_{0.5}La_{0.5}Ti_{1-x}Al_xO_3$ thin films with various x-content labeled as pure, 0.05, 0.10 and 0.15 from Al 2p region.

For the Al 2p region, XPS survey is examined in detail; however, there is a contradiction. If the peaks around 72- 76 eV is assigned to Al 2p states, it is confusing to

see a broad peak of Al 2p for $Li_{0.5}La_{0.5}TiO_3$ composition without Aluminum (pure). Although there is not a clear answer yet, it can be proposed for the various Al doped compositions that the peaks which cannot be identified. This is because of the low weight percentage of Al inside the composition. Therefore, Al 2p signals are not obvious for the identification.

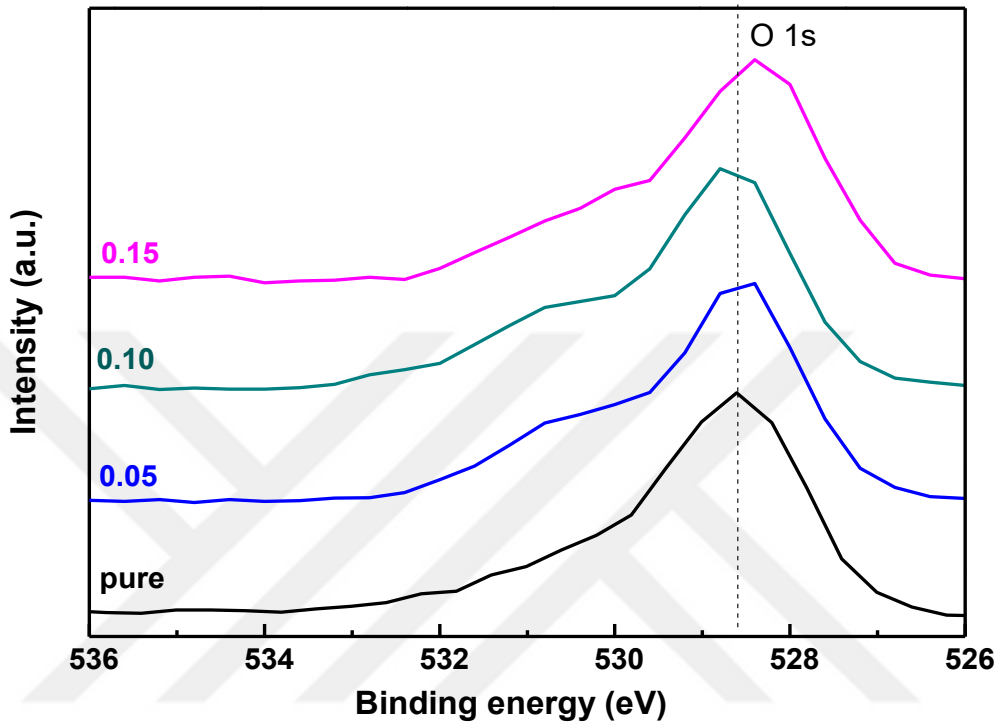

Figure 4.11 XPS spectra of $Li_{0.5}La_{0.5}Ti_{1-x}Al_xO_3$ thin films with various x-content labeled as pure, 0.05, 0.10 and 0.15 from O 1s region.

It is observed for O1s region that there is a slight shift toward lower binding energies for $Li_{0.5}La_{0.5}Ti_{1-x}Al_xO_3$ (x=0.15) thin film composition, which corresponds to Ti-O bond located at 528.6 eV. Bond length will be increased as a result of lower binding energy for x=0.15 composition which can be the explanation for lower ionic conductivity. Decrease of conductivity for x=0.15 composition will be explained by this O 1s signal because decrease in binding energy unlike the proportional substitution. Also, deconvolution of the O1 s peak toward higher binding energies is a sign of surface oxygen adsorption of the thin films. On the other hand, the peak at can be attributed to Ti-O bonding in LLTO structure.

To sum up, peaks of La $3d_{3/2}$ and La $3d_{5/2}$ are shown in Figure 4.8. for different compositions of thin films but there is no such an impressive change that can be observed. However, for the $Li_{0.5}La_{0.5}Ti_{1-x}Al_xO_3$ thin film, Ti $2p_{1/2}$ and Ti $2p_{3/2}$ peaks in Figure 4.9. have shown a slight shift in binding energies toward higher binding energy region with

the increase in x-content. It means that Ti-O bond length will be decreased (Wenzel et al. 2015).

4.2.4. Electrochemical Impedance Spectroscopy (EIS)

Transport properties in polycrystalline solids are strongly affected by microstructure. Impedance spectra usually can provide information directly related to the microstructure (Barsoukov and Macdonald 2005). Much work on correlating microstructure and electrical properties can be directly traced to the pioneering study of Bauerle [1969]. In this section we discuss microstructural models describing grains and grain boundaries of differing phase composition, suspensions of one phase within another, and porosity, while in Section 4.1.3, we give examples of the combined use of IS and electron microscopy. With the two techniques combined, it is possible to derive information of microstructural relevance that is not accessible using one of the techniques alone. It must be realized that the concept of ions in solids as rigid spheres is no more than a useful approximation to a complex quantum wave-mechanical reality. For instance, strong interactions between the outer electrons of neighboring ions, i.e. covalent effects, reduce the ionic radius while the motion of ions in ionic conduction in solids often requires that they should pass through gaps in the structure that are too small for the passage of rigid spheres.

4.2.4.1. Change in Electrical Properties with Increasing Film Thickness, for Different Compositions

For every composition of $Li_{0.5}La_{0.5}Ti_{1-x}Al_xO_3$, thickness dependence of ionic conductivity is investigated for various deposition periods of 15, 30, 60, 90 minutes on ITO substrate with approximately the same deposition rates.

Table 4.8. Deposition time and thickness variables for $Li_{0.5}La_{0.5}TiO_3$ (pure) thin film deposition process

Deposition time (min)	**Thickness (nm)**
15 min	24.50 nm
30 min	36.56 nm
60 min	84.76 nm
90 min	143.87 nm

From deposition time and thickness measurements by the profile meter, deposition rate average is calculated as 0.25 Å/sec.

Table 4.9. Comparison results of the deposition time and conductivity for each composition (except for $Li_{0.5}La_{0.5}Ti_{1-x}Al_xO_3$ (x = 0.15))

$Li_{0.5}La_{0.5}Ti_{1-x}Al_xO_3$ composition (x)	**Thickness dependent conductivity**
pure	$\sigma_{30'} > \sigma_{60'} > \sigma_{15'} > \sigma_{90'}$
x = 0.01	$\sigma_{60'} > \sigma_{30'}$
x = 0.05	$\sigma_{60'} > \sigma_{30'}$
x = 0.10	$\sigma_{60'} > \sigma_{30'} > \sigma_{15'} > \sigma_{90'}$

So, here are the complex impedance spectroscopy results that we calculated ionic conductivity by the formula below;

$$\sigma = \frac{d}{R \times A} \tag{4.8}$$

which is giving directly thin film thickness and conductivity dependence. Although according to the Eqn.(4.8)**;** conductivity is expected to increase with the increase in thickness of the sample. However, experimentally, this is not the case. Experimental results show that the proper thin film thickness for optimum conductivity is 60 minute deposition period, which corresponds to approximately 100-120 nm film thickness. Contradiction between the experimental and theoretical results can be explained by the ion travelling distance and lattice mismatch concepts. For instance, the path that ion is traveling increases by the increase in deposition time/ thickness, which means that the ionic conductivity will be lowered. Furthermore, lattice mismatch between the thin film

and the substrate is another obstacle for the moving ion. So, it can be suggested for lower deposition periods (15', 30') than 60 minute, lattice mismatch is the difficulty that the ion is encountered during its movement from one region to another. However, for the 90 min deposition period, ionic conductivity result decreases, although it can be assumed that the thickness of the thin film can get rid of the lattice mismatch effect for the ion motion, this prediction is misleading. Because in this case (90 min deposition period) causes increase in ionic diffusion path which means that limit of optimum path length is enlarged and lead higher resistive forces acting on travelling ion.

According to analysis of thickness dependence on ionic conductivity, 60 minute deposition time corresponds to the highest conductivity among other deposition periods for most of the $Li_{0.5}La_{0.5}Ti_{1-x}Al_xO_3$ compositions. However, ionic conductivity of $Li_{0.5}La_{0.5}Ti_{1-x}Al_xO_3$ (x=0.15) composition is not included in, since it has different ionic conductivity characteristic, which is not concern here to investigate. On the other hand, it tells us x= 0.15 composition has an excessive amount of Aluminum to promote ionic conduction. Therefore, it is decided $Li_{0.5}La_{0.5}Ti_{0.85}Al_{0.15}O_3$ composition should be interpreted separately from other compositions as it doesn't show enhancement by the Al substitution like others.

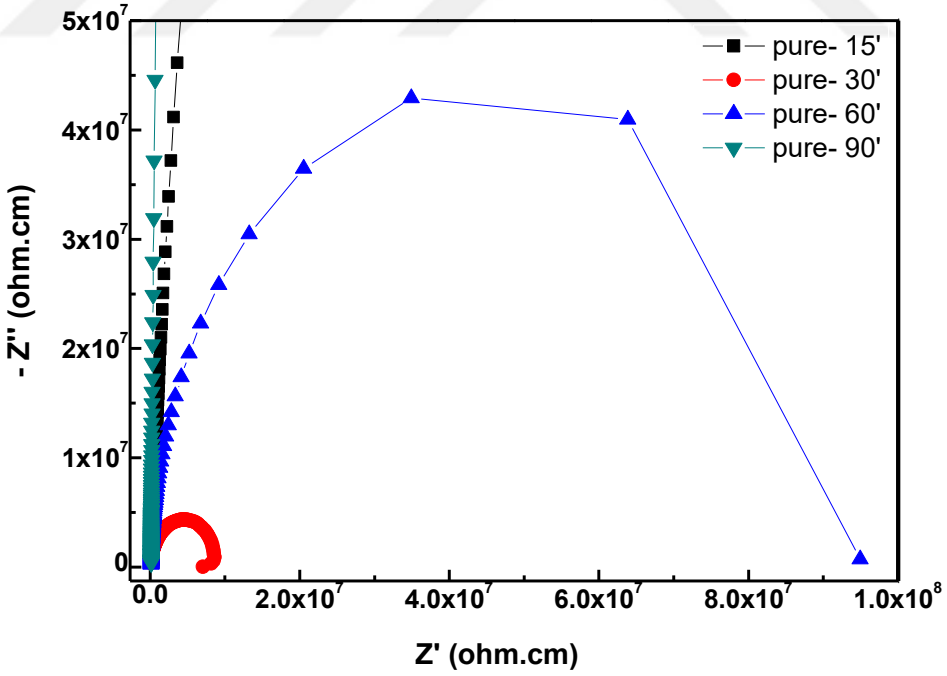

Figure 4.12 $Li_{0.5}La_{0.5}Ti_{1-x}Al_xO_3$ (x = 0.00 – pure) thin film with thicknesses proportional to their deposition times on ITO/SLG s

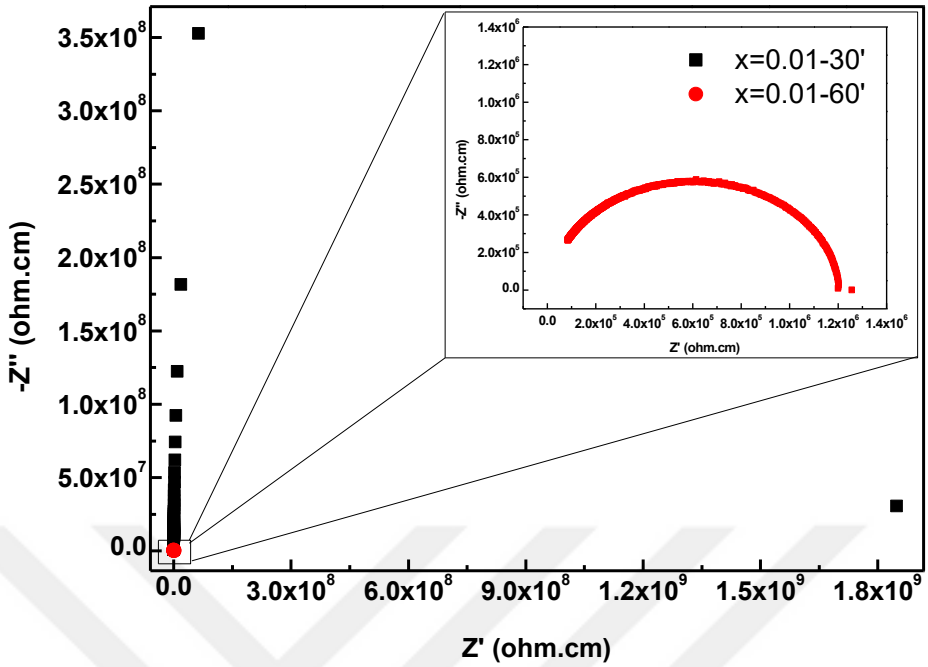

Figure 4.13. $Li_{0.5}La_{0.5}Ti_{1-x}Al_xO_3$ (x = 0.01) thin film with various thicknesses deposited for 30 and 60 minutes on ITO/SLG substrates.

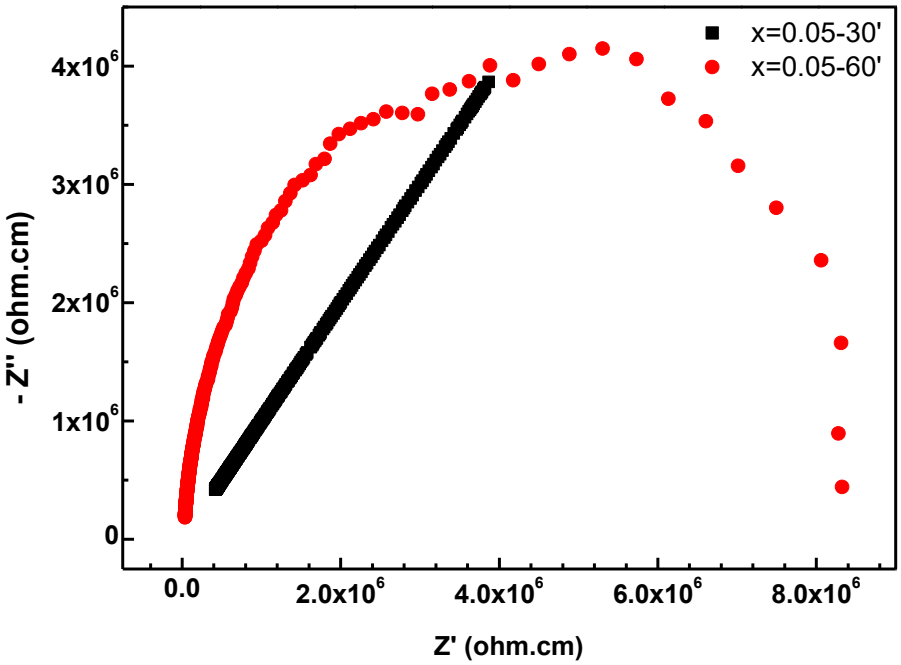

Figure 4.14 $Li_{0.5}La_{0.5}Ti_{1-x}Al_xO_3$ (x = 0.05) thin film with various thicknesses deposited for 30 and 60 minutes on ITO/SLG substrates.

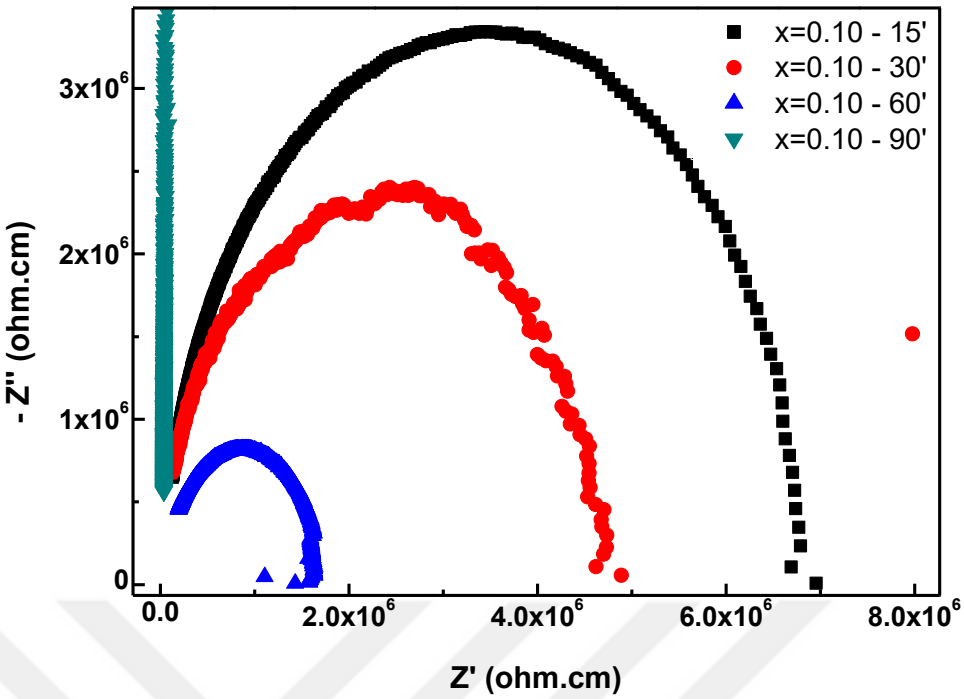

Figure 4.15. $Li_{0.5}La_{0.5}Ti_{1-x}Al_xO_3$ (x = 0. 10) thin films with various thicknesses deposited for 15, 30, 60 and 90 minutes on ITO/SLG substrates

To conclude, the path that ion travel increases by the increase in deposition time/ thickness, which means lower ionic conductivity results. This kind of conductivity decrease is observed for 90 minute deposition, as the long range Li-ion motion. However, for the other deposition periods like 15, 30 and 60 minute, this statement is not valid, because for those deposition periods, which are lower than 60 minute can be interpreted as the thickness of the thin films for 15and 30 minute deposition periods is not enough to get rid of lattice mismatch effect on ionic conduction.

Furthermore, lattice mismatch between the thin film and the substrate is another concern. So, it can be suggested that for shorter deposition periods than 60 minute, lattice mismatch effect on ion migration through this region is strongly detected. Also, this gives us a reason to investigate effect of anneal treatments on those samples that stress factors are common because of the lattice mismatch effect.

4.2.4.2. Effect of Composition on Ionic Conduction

According to composition rather than Al substitution, it should be also mentioned that $Li_{0.5}La_{0.5}TiO_3$ composition is selected consciously, as it is important to study with the best ionic conducting composition to enhance it (Youmbi et al. 2012). Therefore, by the list of different compositions in Table 4.10., $Li_{0.5}La_{0.5}TiO_3$ composition is chosen because of its highest conductivity result among other compositions.

Table 4.10. Room temperature conductivities for different chemical compositions of $LiLaTiO_3$ (Source: Youmbi et al. 2012)

Compound	**Conductivity ($S.cm^{-1}$)**
$Li_{0.5}La_{0.5}TiO_3$	1.7×10^{-3} (σ_{VTF})
	1.9×10^{-3} (σ_{Arr})
$Li_{0.5}La_{0.5}TiO_3$	$\sim 10^{-3}$
$Li_{0.5}La_{0.5}TiO_3$ (cubic)	$\sim 8.2 \times 10^{-4}$
$Li_{0.34}La_{0.51}TiO_{2.94}$	1×10^{-3}
$Li_{0.27}La_{0.59}TiO_3$	$5.8 - 6.8 \times 10^{-4}$
$Li_{0.34}La_{0.56}TiO_3$ (cubic)	1.53×10^{-3}
$Li_{0.34}La_{0.56}TiO_3$ (tetragonal)	6.88×10^{-4}
$Li_{0.10}La_{0.63}TiO_3$	7.9×10^{-5}

However, in this section, main purpose is to clarify the effect of Al substitution with Ti on ionic conductivity. Therefore, thin film samples were grown on ITO/SLG substrates with 60 min deposition period. Then, on the thin film samples Aluminum is evaporated via the mask with various diameter size circle openings. By the shape of the mask, it is aimed to have specific contact areas to calculate conductivity of the covered sample. In Figure 4.16. , impedance spectroscopy results of as deposited (60 minute) samples with various $Li_{0.5}La_{0.5}TiO_3$ (pure), $Li_{0.5}La_{0.5}Ti_{1-x}Al_xO_3$ (x=0.01), $Li_{0.5}La_{0.5}Ti_{1-x}Al_xO_3$ (x=0.05), $L0i_{0.5}La_{0.5}Ti_{1-x}Al_xO_3$ (x=0.10), $Li_{0.5}La_{0.5}Ti_{1-x}Al_xO_3$ (x=0.15) compositions are shown and. calculated ionic conductivity values according to impedance spectroscopy results are tabulated in Table 4.11.

Table 4.11. Ionic conductivities measured at room temperature from different nominal chemical compositions of thin films.

$Li_{0.5}La_{0.5}Ti_{1-x}Al_xO_3$ x	Ionic conductivity ($S.cm^{-1}$)
0 (pure)	1.42×10^{-7}
0.01	7.96×10^{-7}
0.05	9.68×10^{-7}
0.10	2.16×10^{-7}
0.15	0.68×10^{-7}

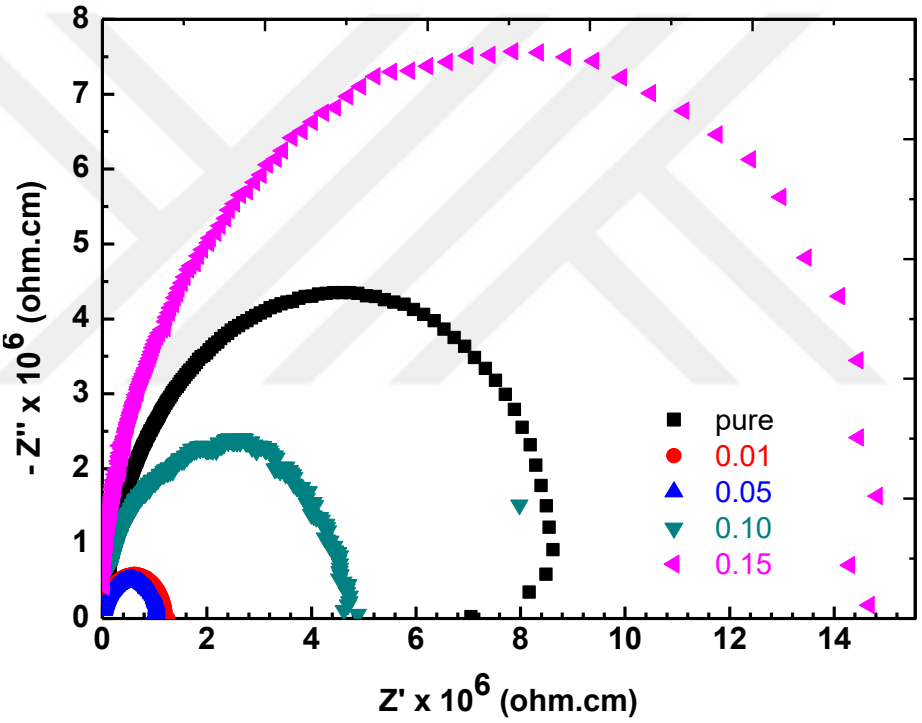

Figure 4.16. The complex impedance spectra of as deposited $Li_{0.5}La_{0.5}Ti_{1-x}Al_xO_3$ thin films with different Al contents.

It can be inferred from the complex impedance spectra that the addition of Al has up to some content, positive effects for ionic conduction. All compositions with some content of Al substitution (except for x=0.15) show enhancement in ionic conduction compared to $Li_{0.5}La_{0.5}TiO_3$ composition without Aluminum as it can be seen from the Figure 4.17.

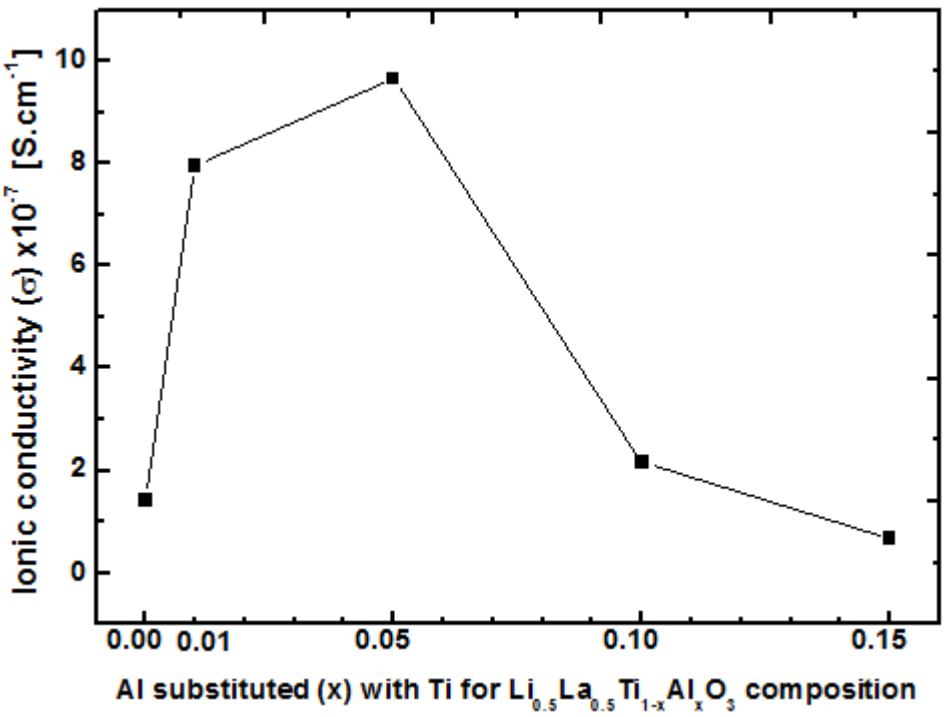

Figure 4.17 Schematic representation of Aluminum substituted content (x) versus ionic conductivity results obtained from thin film samples.

To understand the reason for this effect, it is important to know LLTO electrolyte material, that we examine, has ABO_3 type perovskite structure. A is used to represent Li/ La and B is used for Ti for LLTO compound.

A factor that lead increase in conductivity is the size of the ionic radius difference between Ti^{+4} (r(VI)Ti^{+4}=0.605 Å) and Al^{+3} ion (r(IV)Al^{+3}=0.53 Å). Smaller ionic radius will have lower effect on conduction. Furthermore, difference in ionic radii will lead distortion in [Ti/Al-O_6] octahedral that can provide suitable A-O and B-O distance for the conduction. In other words, According to Morata-Orrantia *et al*., substitution of Aluminum with Ti causes increase in A-O distance and at the same time shortening of B-O distance, that can facilitate ion motion (Morata-Orrantia, Garcıa-Martin, and Alario-Franco 2003).

In our research, effects of the Al substitution on structure can be examined by the SEM images shown in Figure 4.6. . For x = 0.01 composition, it can be seen clearly that the grains are not separate, have connected pathways, that tell us the grain boundary connectivity is increased.

4.2.4.3. Effect of Anneal Temperature on Different Compositions

Effect of anneal temperature on structure is investigated if it has beneficial results on ionic conductivity. Therefore, all thin film samples are grown on ITO/SLG substrates for 60 minute deposition period. Then, each thin film composition of $Li_{0.5}La_{0.5}Ti_{1-x}Al_xO_3$ is subjected to anneal temperatures of 100 ˚C, 200 ˚C, 300 ˚C and 400 ˚C for 2 hours in air environment. Heating rate for each temperature step is 5 ˚C/min and let it natural cool down after 2 hours hold at anneal temperature. Below the results of impedance spectroscopy and calculated ionic conductivities for each composition and anneal temperature is tabulated. Furthermore, SEM images of those thin film samples are shown in Table 4.12 and examined to find any relationship to explain any regular effect. However, effect of anneal temperature is a little bit complex, as the stress- strain relaxations are not the same for every sample but can be put forward as a reason for increase in conduction. Although there is not a proper relationship between the anneal temperature and ionic conductivity, it has a beneficial effect on conduction, which can be justified by results of improved ionic conductivity after annealing.

Table 4.12. Complex impedance plots of each $Li_{0.5}La_{0.5}Ti_{1-x}Al_xO_3$ composition with anneal treatment

Complex Impedance Plots of Anneal Treatment	**Anneal temperature**	**Conduc-tivity**
Pure		
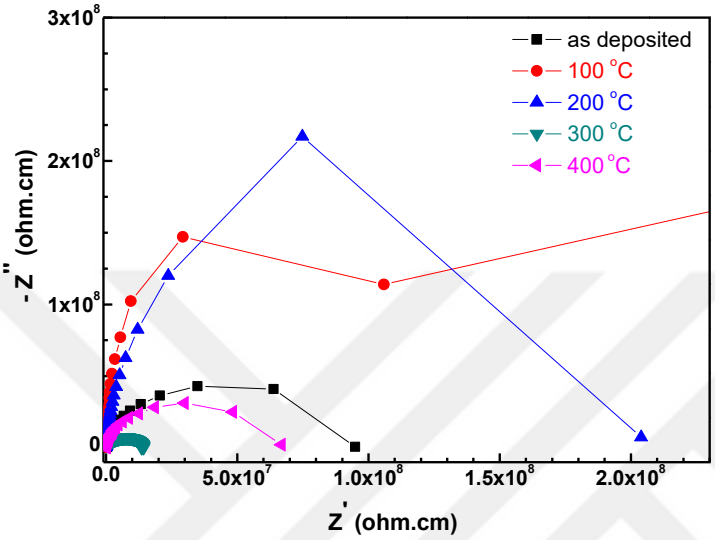	As deposited	1.04 x 10^{-8}
	100˚C	7.92 x 10^{-9}
	200˚C	4.88 x 10^{-9}
	300˚C	7.41 x 10^{-8}
	400˚C	1.49x 10^{-8}
x = 0.01	**Anneal temperature**	**Conduc-tivity**
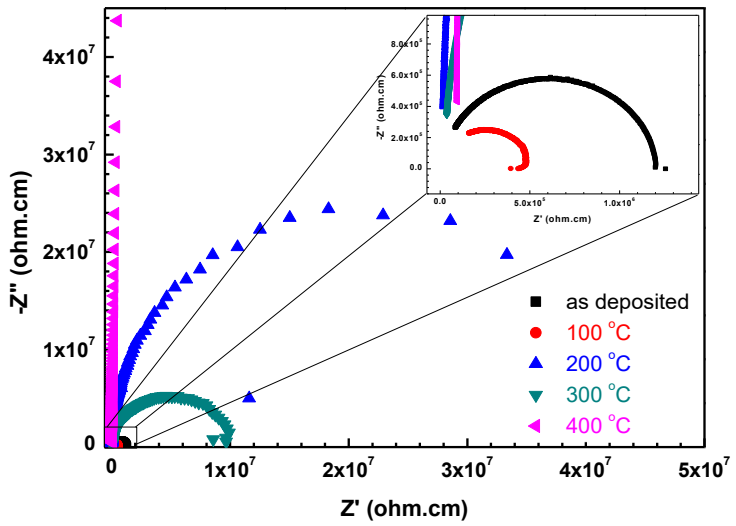	As deposited	7.96 x 10-7
	100˚C	2.36 x 10^{-6}
	200˚C	0.85 x 10^{-7}
	300˚C	1.03 x 10^{-7}
	400˚C	very low

(cont. on next page)

Table 4.12. (cont.)

x = 0.05	Anneal temperature	Conduc-tivity
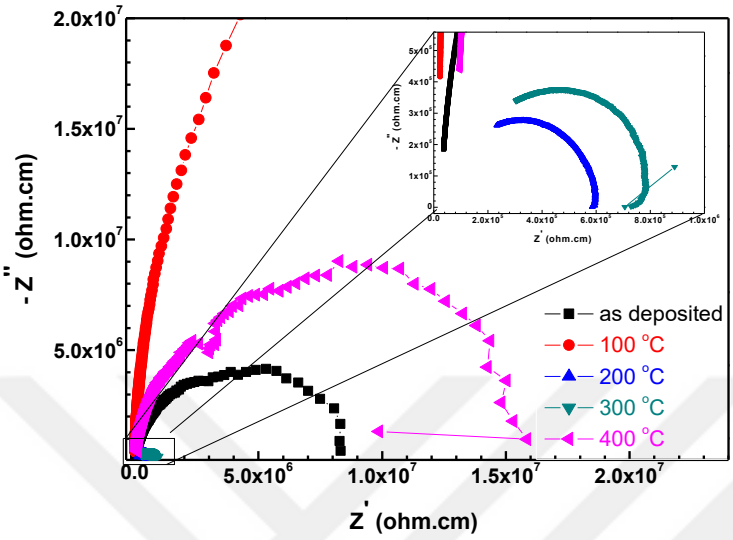	As deposited	0.12 x 10^{-6}
	100°C	0.01 x 10^{-6}
	200°C	1.70 x 10^{-6}
	300°C	1.42 x 10^{-6}
	400°C	0.06 x 10^{-6}

x = 0.10	Anneal temperature	Conduc-tivity
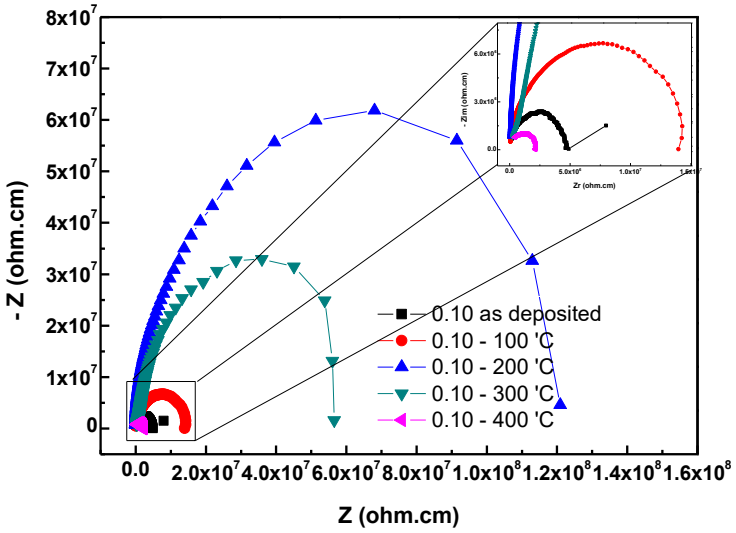	As deposited	2.16 x 10^{-7}
	100°C	7.15 x 10^{-7}
	200°C	8.15x 10^{-9}
	300°C	1.75 x 10^{-8}
	400°C	4.51 x 10^{-7}

(cont. on next page)

Table 4.12. (cont.)

x = 0.15	Anneal temperature	Conduc-tivity
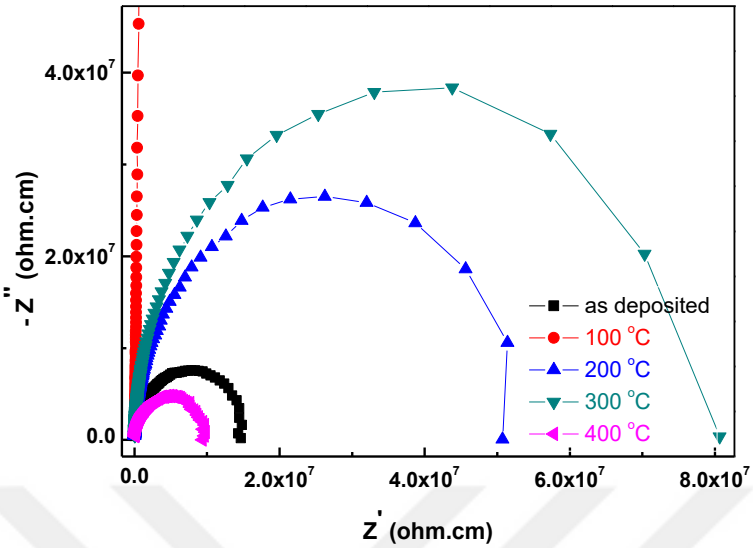	As deposited	6.48 x 10^{-8}
	100˚C	very low
	200˚C	1.97 x 10^{-8}
	300˚C	1.24 x 10^{-8}
	400˚C	1.10 x 10^{-7}

4.2.4.4. Arrhenius Plot

Impedance spectroscopy measurements were performed in the frequency range from 0.1 Hz to 200 kHz. In order to determine activation energy barrier for the ion migration from one side to other, temperature dependent measurements were done within the same frequency range by changing temperature from 298 K to 363 K.

After the measurements for each temperature step, there is a conductivity result that we have obtained for $Li_{0.5}La_{0.5}Ti_{0.95}Al_{0.05}O_3$ thin film sample, which has the highest ionic conductivity result among other investigated compositions. So, temperature dependence of $Li_{0.5}La_{0.5}Ti_{0.95}Al_{0.05}O_3$ thin film shows non-Arrhenius behavior that can be seen in Figure 4.18**.** It is observed after 333 K, slope of the line will change which means that change in activation energy barrier. In other words, the calculations show that Li-ion conduction mechanism is changed for the temperatures above 333 K (60 °C.) that appear in two activation energies as 0.08 eV for T < 333 K, 0.15 eV for T > 333 K. By the increase in temperature, mobility of Li-ions will be enhanced to promote ionic conduction; however, after some degree of temperature increase (T > 333 K), it will cause scattering of Li-ions because of the increase in thermal vibrations of adjacent atoms, which results in higher activation energy barriers for ions to overcome for the conduction.

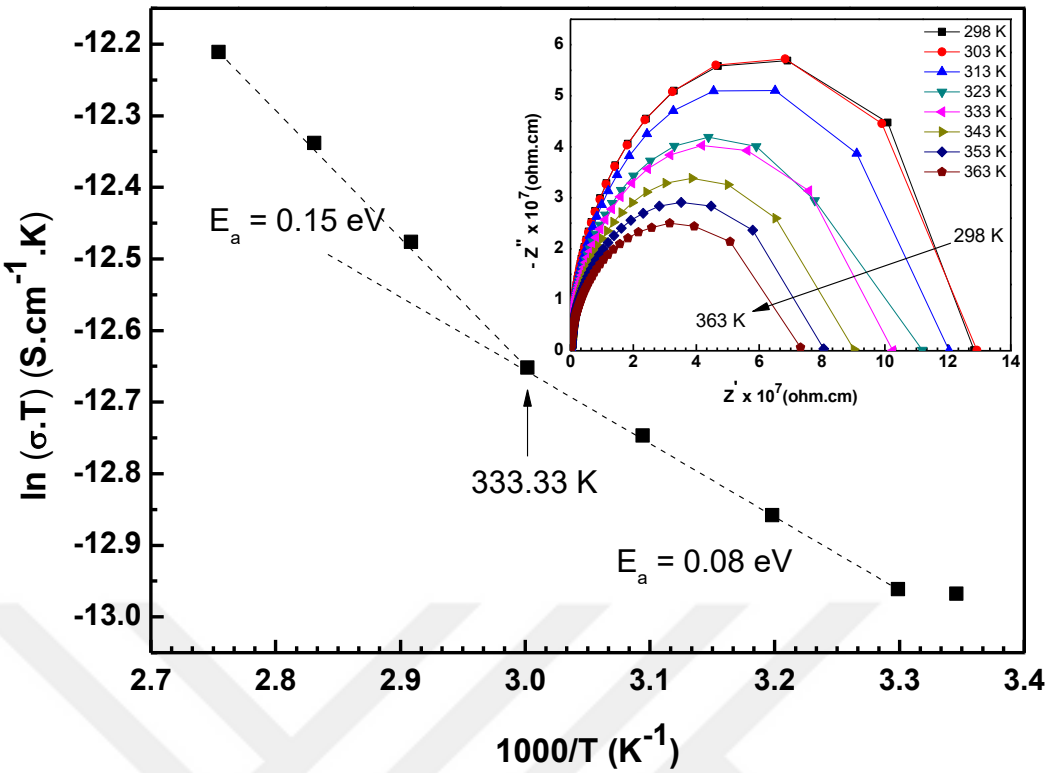

Figure 4.18 Arrhenius plots of the conductivity as a function of 1000/T for LLTAlO (x=0.05) annealed at 300 K and the inset shows complex impedance curves at each temperature.

To conclude, conduction mechanism will change according to applied frequency and temperature range depending on the material's microstructure and chemical components. At low temperatures, grain boundary conduction was dominated by easy paths while at high temperatures overtook the easy path mechanism. If this interpretation is correct, transition between the easy path and true grain boundary conduction in the same system would be clear indication that Impedance spectroscopy can reveal deep information, when performed over the necessary range of frequency and temperature (Barsoukov and Macdonald 2005).

4.2.4.5. Frequency Dependent Conductivity Measurements

The origin of frequency dependence of the conductivity is due to relaxation of the ionic atmosphere after the movement of the particle.

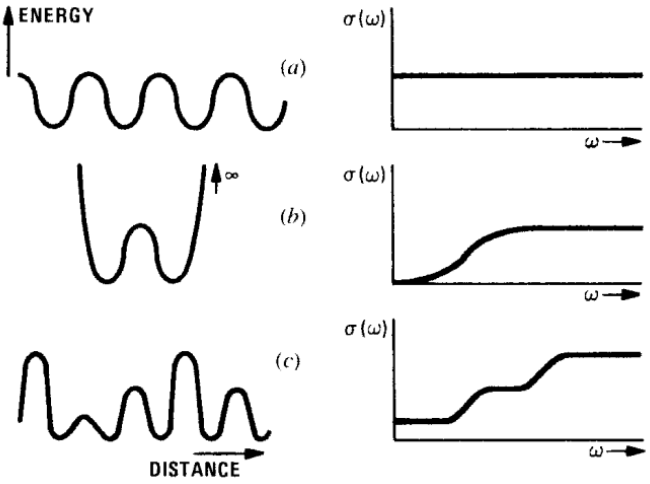

Figure 4.19. Frequency dependence of the hopping conductivity for different potential energy profiles: (a) periodic constant activation energy, (b) single bi-well, (c) potential profile with multiple activation energies (Source: Barsoukov and Macdonald 2005)

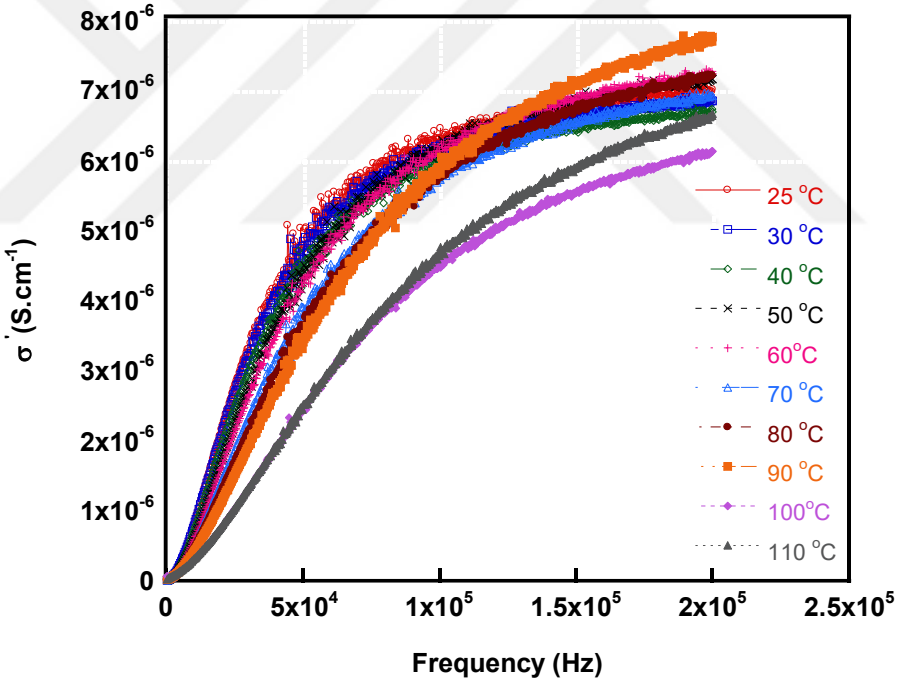

Figure 4.20. Real part (σ') of complex conductivity as a function of frequency for $Li_{0.5}La_{0.5}Ti_{1-x}Al_xO_3$ (x=0.05) annealed at 300 ˚C from 25 ˚C to 110 ˚C in 0.1 Hz – 200 kHz frequency range

In Figure 4.19., it is shown conductivity results as a function of the frequency which we can also plot our data as in Figure 4.20. By the light of this common behavior against frequency, expected potential energies can be determined for thin film $Li_{0.5}La_{0.5}Ti_{1-x}Al_xO_3$ (x=0.05) sample annealed at 300 ˚C. For our experimental study, frequency dependent conductivity results show single bi-well potential barrier for the

ionic conduction. Within the temperature range it gives the same response to 0.1 Hz – 200 kHz frequency, although it is interesting that it changes its activation energy by the increase in temperature. So, there is turning point for the curve of σ vs ω plot, which tells that up to a frequency value, relaxation of dipoles are faster, but after some point of higher frequency, polarizations will not have time to build up; therefore, the curvature of conductivity slows down at higher frequencies.

CHAPTER 5

CONCLUSION

Firstly, pure and Al doped $Li_{0.5}La_{0.5}Ti_{1-x}Al_xO_3$ targets were successfully synthesized by conventional solid state reactions. Then, RF magnetron sputtering technique is used to sputter the thin films of LLTO. Later, structural, morphological, and electrical properties were tried to be characterized by XRD, Raman spectroscopy, SEM, and impedance spectroscopy analyses respectively. So, based on the obtained results following remarks can be concluded as follows:

- Compared to $Li_{0.5}La_{0.5}TiO_3$ (pure) composition, other Al (x) substituted amounts has given positive effect on conduction except for $Li_{0.5}La_{0.5}Ti_{1-x}Al_xO_3$ (x = 0.15) composition. Highest ionic conductivity result is obtained from $Li_{0.5}La_{0.5}Ti_{1-x}Al_xO_3$ (x = 0.05) composition as ~10^{-6} S/cm, which is 10^2 higher than $Li_{0.5}La_{0.5}TiO_3$ (pure) composition. $Li_{0.5}La_{0.5}Ti_{1-x}Al_xO_3$ (x = 0.01) takes the second place for the highest ionic conduction and after that x = 0.10 composition comes compared to $Li_{0.5}La_{0.5}TiO_3$ (pure), but $Li_{0.5}La_{0.5}Ti_{1-x}Al_xO_3$ (x = 0.15) composition has the lowest ionic conduction result. So, it is obvious that over addition of Al_2O_3 would decrease the effective pathways for Li-ion conduction. It can be suggested that over addition violates open and amorphous structure of the thin films.
- Effect of thickness on ionic conduction and surface morphology is investigated in order to find an optimum thickness for the ionic conduction. And it is understood that it has an optimum thickness value about 84.76 nm that corresponds to approximately 60 minute deposition. It can be proposed that thin films with ~120 nm thickness were under the effect of lattice mismatch. Lower ionic conductivity results from lower thicknesses is a sign of it. However, this should not lead to an idea that going to higher thicknesses will result in higher ionic conductivities. Thus, this is not the case. Experimental results show that thicknesses correspond to 140 nm (90 min. deposition), do not give higher ionic conductivity result compared to 84 nm (60 min. deposition). Therefore, it is decided that for each $Li_{0.5}La_{0.5}Ti_{1-x}Al_xO_3$ composition, 90 min. deposition thickness is not proper. So,

in addition to lattice mismatch, the path that Li-ion travel is another important factor. As the thickness is increased, the distance that ion will travel also increases, which leads Li-ion to encounter more obstacles. Therefore, 60 min deposition giving approximately 85 nm thin film thickness is the most suitable thickness value for higher ionic conduction.

- Also, the effect of anneal treatment on thin film samples with 60 minute deposition for every composition is investigated. However, the results do not show a trend-line with the annealing temperature. But in each case, annealing has a positive effect on conduction. For instance, for $Li_{0.5}La_{0.5}Ti_{1-x}Al_xO_3$ (x = 0.01) composition annealed at 100 °C, has the highest ionic conduction of all, as $\sigma = 2.36\times 10^{-6}\ S/cm$, which has reached highest conductivity value of $Li_{0.5}La_{0.5}Ti_{1-x}Al_xO_3$ (x = 0.05) composition.
- Besides, temperature dependent complex impedance spectra results were measured for the highest ionic conducting compound, which is $Li_{0.5}La_{0.5}Ti_{0.95}Al_{0.05}O_3$ composition annealed at 300 °C. From these measurements, temperature dependent conductivity results were calculated to find activation barrier for the Li-ion hopping. So, the calculations show that Li-ion conduction mechanism is changed for the temperatures above 333 K (60 °C) that appear in two activation energy results as 0.08 eV for T < 333 K, and 0.15 eV for T > 333 K. By the increase in temperature, mobility of Li-ions will be enhanced to promote ionic conduction; however, after some degree of increase in temperature (T > 333 K), it will cause scattering of Li-ions because of the increase in thermal vibrations of adjacent atoms, which results in higher activation energy barriers for ions to overcome for the conduction.

More investigations may be done on different x- compositions of $Li_{0.5}La_{0.5}Ti_{1-x}Al_xO_3$ for $0.01 < x < 0.05$ region, as they will provide higher ionic conductivity results. Grazing incidence XRD and Raman analysis should be done for further investigations for the structural determination of the thin films, since it is still an unknown. In addition, XPS measurements can be analyzed to find possible phases and calculate the exact compositions of thin films. Besides, pellets can be prepared to examine $Li_{0.5}La_{0.5}Ti_{1-x}Al_xO_3$ material in bulk form to make comparison in between the thin film and bulk structure of LLTO.

REFERENCES

Antoniassi, B., A. H M González, S. L. Fernandes, and C. F O Graeff. 2011. "Microstructural and Electrochemical Study of La0.5Li 0.5TiO3." *Materials Chemistry and Physics* 127 (1–2). Elsevier B.V.: 51–55. doi:10.1016/j.matchemphys.2010.12.021.

Barsoukov, Evgenij, and J. Ross Macdonald. 2005. *Impedance Spectroscopy*. *Impedance Spectroscopy: Theory, Experiment, and Applications*. doi:10.1002/0471716243.

Beiser. 2003. "Concepts_of_Modern_Physics_by_Beiser.pdf."

Belous, a. 1996. "Synthesis and Electrophysical Properties of Novel Lithium Ion Conducting Oxides." *Solid State Ionics* 90 (1–4): 193–96. doi:10.1016/S0167-2738(96)00406-7.

Chen, RenJie J., Wei Liang, HaiQin Q. Zhang, Feng Wu, and Li Li. 2012. "Preparation and Performance of Novel LLTO Thin Film Electrolytes for Thin Film Lithium Batteries." *Chinese Science Bulletin* 57 (32): 4199–4204. doi:10.1007/s11434-012-5292-y.

Conway, B. 1991. "Transition from 'Supercapacitor' to 'Battery' Behavior in Electrochemical Energy Storage." *J. Electrochem. Soc.* 138 (6): 1539–48. doi:10.1149/1.2085829.

DeHoff, Robert. 2006. *Thermodynamics in Materials Science*. New York,NY: Taylor and Francis Group

Demirhan, Yasemin. 2011. "Fabrication of Double Mesa Structures From Superconducting $Bi_2Sr_2CaCu_2O_{8+D}$ by E-Beam Lithography for Terahertz Emission A Thesis Submitted to in Physics," no. July.

García-Martín, Susana, Ulises Amador, Ainhoa Morata-Orrantia, Juan Rodríguez-Carvajal, and Miguel Ángel Alario-Franco. 2009. "Structure, Microstructure, Composition and Properties of Lanthanum Lithium Titanates and Some Substituted Analogues." *Zeitschrift Fur Anorganische Und Allgemeine Chemie* 635 (15): 2363–73. doi:10.1002/zaac.200900124.

Geng, Hongxia, Ao Mei, Yuanhua Lin, and Cewen Nan. 2009. "Effect of Sintering Atmosphere on Ionic Conduction and Structure of $Li_{0.5}La_{0.5}TiO_3$ Solid Electrolytes." *Materials Science and Engineering B: Solid-State Materials for Advanced Technology* 164 (2): 91–95. doi:10.1016/j.mseb.2009.07.011.

Gülen, Sena. 2015. "$Li_xLa_yTiO_3$ Electrolyte For All-Solid State Li-Ion Batteries A Thesis Submitted in Physics."

Huggins, R. A. 2002. "Simple Method to Determine Electronic and Ionic Components of the Conductivity in Mixed Conductors a Review." *Ionics* 8: 300–313. doi:10.1007/BF02376083.

Inaguma, Yoshiyuki, Liquan Chen, Mitsuru Itoh, and Tetsuro Nakamura. 1994. "Candidate Compounds with Perovskite Structure for High Lithium Ionic Conductivity." *Solid State Ionics* 70–71 (PART 1): 196–202. doi:10.1016/0167-2738(94)90309-3.

Inaguma, Yoshiyuki, Chen Liquan, Mitsuru Itoh, Tetsuro Nakamura, Takashi Uchida, Hiromasa Ikuta, and Masataka Wakihara. 1993. "High Ionic Conductivity in Lithium Lanthanum Titanate." *Solid State Communications* 86 (10): 689–93. doi:10.1016/0038-1098(93)90841-A.

Koseoglu, Hasan, Fulya Turkoglu, Metin Kurt, Mutlu D. Yaman, Fatime G. Akca, Gulnur Aygun, and Lutfi Ozyuzer. 2015. "Improvement of Optical and Electrical Properties of ITO Thin Films by Electro-Annealing." *Vacuum* 120 (September): 8–13. doi:10.1016/j.vacuum.2015.06.027.

Laguna, M. A., M. L. Sanjuan, A. Varez, and J. Sanz. 2002. "Lithium Dynamics and Disorder Effects in the Raman Spectrum of La(2-x)/3LixTiO3." *Physical Review B - Condensed Matter and Materials Physics* 66 (5): 543011–17. doi:10.1103/PhysRevB.66.054301.

Li, Chi Lin, Bin Zhang, and Zheng Wen Fu. 2006. "Physical and Electrochemical Characterization of Amorphous Lithium Lanthanum Titanate Solid Electrolyte Thin-Film Fabricated by E-Beam Evaporation." *Thin Solid Films* 515 (4): 1886–92. doi:10.1016/j.tsf.2006.07.026.

Linnala, Mikko. 1990. "Master Thesis." *Mycotoxin Research* 6 (2): 100. doi:10.1007/BF03192151.

Lvovich, Vadim F. 2012. *Impedance Spectroscopy: Applications to Electrochemical and Dielectric Phenomena*. *Impedance Spectroscopy: Applications to Electrochemical and Dielectric Phenomena*. doi:10.1002/9781118164075.

Morata-Orrantia, Ainhoa, Susana García-Martín, Emilio Morán, and Miguel Ángel Alario-Franco. 2002. "A New La2/3LixTi1-xAlxO3 Solid Solution: Structure, Microstructure, and Li+ Conductivity." *Chemistry of Materials* 14 (7): 2871–75. doi:10.1021/cm011149s.

Morata-Orrantia, Ainhoa, Susana Garcıa-Martin, and Miguel A. Alario-Franco. 2003. "Optimization of Lithium Conductivity in La / Li Titanates." *Chem. Mater.* 15 (21): 3991–95.

Moulson A.J. 2014. "Electroceramic." *Igarss 2014*, no. 1: 1–5. doi:10.1007/s13398-014-0173-7.2.

Omanda, H M, H Gnanga, P Soulounganga, R Ondo Ndong, A Eya, Laboratoire Pluridisciplinaire, and Ecole Normale Supérieure. 2014. "Raman Scattering Study of La2/3-xLi3x□1/3-2xTiO3 : Relationship between Spectra Parameters and Amount of Lithium" 3 (1): 3476–81.

Pham, Q, C Bohnke, and O Bohnke. 2004. “Effect of Surface Treatments on Li0.30Ln0.57TiO3 (Ln = La, Nd) Perovskite Ceramics: An X-Ray Photoelectron Spectroscopy Study.” *Surface Science* 572 (2): 375–84. doi:10.1016/j.susc.2004.09.012.

Raistrick, I.D., C. Ho, and R.A. Huggins. 1976. “Ionic Conductivity of Some Lithium Silicates and Aluminosilicates.” *Journal of The Electrochemical Society* 123 (10): 1469–76. doi:10.1149/1.2132621.

Stoynov, Z B, D E Vladikova, and Bulgarian Academy. 2009. “Basics of Electrochemical Impedance Spectroscopy,” no. 1: 632–42.

Stramare, S., V. Thangadurai, and W. Weppner. 2003. “Lithium Lanthanum Titanates: A Review.” *Chemistry of Materials* 15 (21): 3974–90. doi:10.1021/cm0300516.

Tarascon, J M, and M Armand. 2001. “Issues and Challenges Facing Rechargeable Lithium Batteries.” *Nature* 414 (6861): 359–67. doi:10.1038/35104644.

Trong, Le Dinh, Tran Thi Thao, and Nguyen Nang Dinh. 2015. “Characterization of the Li-Ionic Conductivity of La(2/3−x)Li3xTiO3 Ceramics Used for All-Solid-State Batteries.” *Solid State Ionics* 278. Elsevier B.V.: 228–32. doi:10.1016/j.ssi.2015.05.027.

Wenzel, Sebastian, Thomas Leichtweiss, Dominik Krüger, Joachim Sann, and Jürgen Janek. 2015. “Interphase Formation on Lithium Solid Electrolytes - An in Situ Approach to Study Interfacial Reactions by Photoelectron Spectroscopy.” *Solid State Ionics* 278. Elsevier B.V.: 98–105. doi:10.1016/j.ssi.2015.06.001.

Youmbi, B. Sitamtze, Serge Zékeng, Samuel Domngang, Florent Calvayrac, and Alain Bulou. 2012. “An Ab Initio Molecular Dynamics Study of Ionic Conductivity in Hexagonal Lithium Lanthanum Titanate Oxide $La_{0.5}Li_{0.5}TiO_3$.” *Ionics* 18 (4): 371–77. doi:10.1007/s11581-012-0662-7.

Zheng, Z., H. Fang, F. Yang, Z.-K. Liu, and Y. Wang. 2014. “Amorphous $LiLaTiO_3$ as Solid Electrolyte Material.” *Journal of the Electrochemical Society* 161 (4): A473–79. doi:10.1149/2.006404jes.